

Extended radio emission in MOJAVE Blazars: Challenges to Unification

P. Kharb^{1,2*}

Dept of Physics, Rochester Institute of Technology, Rochester, NY 14623

kharb@cis.rit.edu

M. L. Lister²

Dept of Physics, Purdue University, 525 Northwestern Ave, West Lafayette, IN 47907

and

N. J. Cooper²

ABSTRACT

We present the results of a study on the kiloparsec-scale radio emission in the complete flux density limited MOJAVE sample, comprising 135 radio-loud AGNs. New 1.4 GHz VLA radio images of six quasars, and previously unpublished images of 21 blazars, are presented, along with an analysis of the high resolution (VLA A-array) 1.4 GHz emission for the entire sample. While extended emission is detected in the majority of the sources, about 7% of the sources exhibit only radio core emission. We expect more sensitive radio observations, however, to detect faint emission in these sources, as we have detected in the erstwhile “core-only” source, 1548+056. The kiloparsec-scale radio morphology varies widely across the sample. Many BL Lacs exhibit extended radio power and kiloparsec-scale morphology typical of powerful FRII jets, while a substantial number of quasars possess radio powers intermediate between FRIs and FRIIs. This poses challenges to the simple radio-loud unified scheme, which links BL Lacs to FRIs and quasars to FRIIs. We find a significant correlation between extended radio emission and parsec-scale jet speeds: the more radio powerful sources possess faster jets. This indicates that the 1.4 GHz (or low frequency) radio emission is indeed related to jet kinetic power. Various properties such as extended radio power and apparent parsec-scale jet speeds vary smoothly between different blazar subclasses, suggesting that, at least in terms of radio jet properties, the distinction between quasars and BL Lac objects, at an emission-line equivalent width of 5Å is essentially an arbitrary one. While the two blazar subclasses

display a smooth continuation in properties, they often reveal differences in the correlation test results, when considered separately. This can be understood if, unlike quasars, BL Lacs do not constitute a homogeneous population, but rather include both FRI and FRII radio galaxies for their parent population. It could also just be due to small number statistics. We find that the ratio of the radio core luminosity to the k -corrected optical luminosity (R_v) appears to be a better indicator of orientation for this blazar sample, than the traditionally used radio core prominence parameter (R_c). Based on the assumption that the extended radio luminosity is affected by the kiloparsec-scale environment, we define the ratio of extended radio power to absolute optical magnitude (L_{ext}/M_{abs}) as a proxy for environmental effects. Trends with this parameter suggest that the parsec-scale jet speeds and the parsec-to-kiloparsec jet misalignments are not affected by the large-scale environment, but are more likely to depend upon factors intrinsic to the AGN, or its local parsec-scale environment. The jet speeds could, for instance, be related to the black hole spins, while jet misalignments could arise due to the presence of binary black holes, or kicks imparted to black holes via black hole mergers, consistent both with radio morphologies resembling precessing jet models observed in some MOJAVE blazars, and the signature of a 90° bump in the jet misalignment distribution, attributed to low-pitch helical parsec-scale jets in the literature. We suggest that some of the extremely misaligned MOJAVE blazar jets could be “hybrid” morphology sources, with an FRI jet on one side and an FRII jet on the other. Finally, it is tempting to speculate that environmental radio boosting (as proposed for Cygnus A) could be responsible for blurring the Fanaroff-Riley dividing line in the MOJAVE blazars, provided a substantial fraction of them reside in dense (cluster) environments.

Subject headings: galaxies: active — quasars: general — BL Lacertae objects: general — radio continuum: galaxies

1. INTRODUCTION

Radio-loud active galactic nuclei (AGNs) that are characterised by extreme variability in their radio cores, high and variable polarization, superluminal jet speeds and compact

¹*Major part of this work completed at Department of Physics, Purdue University, 525 Northwestern Ave, West Lafayette, IN 47907

radio emission, are collectively referred to as ‘blazars’ (Angel & Stockman 1980). Blazars comprise flat-spectrum radio-loud quasars and BL Lac objects. Their extreme characteristics have commonly been understood to be a consequence of relativistic beaming effects due to a fast jet aligned close to our line of sight (Blandford & Konigl 1979).

The radio-loud unified scheme postulates that quasars and BL Lacs are the beamed end-on counterparts of the Fanaroff-Riley (FR, Fanaroff & Riley 1974) type II and type I radio galaxies, respectively (Urry & Padovani 1995). The relatively lower radio luminosity FRI radio galaxies are referred to as “edge-darkened” since their brightest lobe emission lies closer to the radio cores and fades further out, while the higher radio luminosity FRII radio galaxies are “edge-brightened” because of the presence of bright and compact hot spots where the kpc-scale jets terminate. This definition turns out to be useful for FRI-FRII classification when hot spots are not clearly delineated (*cf.* §3.2).

The Fanaroff-Riley dichotomy has been proposed to arise due to differences in one or more of the following properties: host galaxy environment (Prestage & Peacock 1988) and jet-medium interaction (Bicknell 1995), jet composition (Reynolds et al. 1996), black hole mass (Ghisellini & Celotti 2001), black hole spin (Meier 1999), accretion rate and/or mode (Baum et al. 1995; Ghisellini & Celotti 2001). Many recent findings are, however, posing challenges for the standard unified scheme. These include the discovery of FRI quasars (Heywood et al. 2007), FRII BL Lacs (Landt et al. 2006), and “hybrid” radio morphology sources with an FRI jet on one side of the core and an FRII jet on the other (Gopal-Krishna & Wiita 2000). One of the primary cited differences between quasars and BL Lacs has been the presence of strong, broad emission lines in the quasar spectra and their apparent absence in BL Lacs. Stickel et al. (1991) and Stocke et al. (1991) have defined the distinction between BL Lacs and quasars at an emission line equivalent width of 5\AA . However, this distinction has been questioned (e.g., Scarpa & Falomo 1997; Urry 1999; Landt et al. 2004), and it is known that some BL Lacs have a broad-line region (e.g., Miller et al. 1978; Stickel et al. 1991; Vermeulen et al. 1995; Corbett et al. 1996).

In this paper, we examine the unified scheme and FR dichotomy in the MOJAVE² sample of blazars. MOJAVE is a long-term program to monitor radio brightness and polarization variations in the jets associated with active galaxies visible in the northern sky on parsec-scales with Very Long Baseline Interferometry (VLBI) (Lister et al. 2009a). The MOJAVE sample consists of 135 sources satisfying the following criteria: (1) J2000.0 declination $> -20^\circ$; (2) galactic latitude $|b| > 2.5^\circ$; (3) VLBA 2 cm correlated flux density

²Monitoring Of Jets in Active galactic nuclei with VLBA Experiments.
<http://www.physics.purdue.edu/MOJAVE/>

exceeding 1.5 Jy (2 Jy for declination south of 0°) at any epoch between 1994.0 and 2004.0. Of the 135 AGNs, 101 are classified as quasars, 22 as BL Lac objects, and eight as radio galaxies of mostly the FRII-type. Four radio sources are yet to be identified on the basis of their emission line spectra and have no redshift information. Overall, eight sources (four BL Lacs and four unidentified) have unknown or unreliable redshifts. Based on the synchrotron peak in the spectral energy distributions (SEDs), BL Lacs have been divided into low, high, and intermediate energy peaked classes (LBLs, HBLs, IBLs, Padovani & Giommi 1995; Laurent-Muehleisen et al. 1999). All but three MOJAVE BL Lacs are classified as LBLs (see Nieppola et al. 2006, NED). The three BL Lacs, *viz.*, 0422+004, 1538+149 and 1807+698, are classified as IBLs. There are no HBLs in the MOJAVE sample.

The compact flux density selection criteria of the MOJAVE sample biases it heavily toward highly beamed blazars with high Lorentz factors and small viewing angles. While relativistic boosting effects are likely to dominate the source characteristics, the extensive multi-epoch and multi-wavelength data available for the MOJAVE sample on both parsec- and kiloparsec-scales, provides us with unique constraints to test the unified scheme. Throughout the paper, we adopt the cosmology in which $H_0=71 \text{ km s}^{-1} \text{ Mpc}^{-1}$, $\Omega_m=0.27$ and $\Omega_\Lambda=0.73$. Spectral index, α , is defined such that, flux density S_ν at frequency ν , is $S_\nu \propto \nu^{-\alpha}$.

2. DATA REDUCTION AND ANALYSIS

We observed seven MOJAVE quasars at 1.46 GHz with the Very Large Array (VLA, Napier et al. 1983) in the A-array configuration (typical synthesized beam $\sim 1.5''$) on June 30, 2007 (Program ID:AC874). Sixty MOJAVE sources were previously observed by us with the VLA A-array and presented in Cooper et al. (2007). Data for the remaining sources were reduced directly using archival VLA A-array data, or obtained through published papers. The data reduction was carried out following standard calibration and reduction procedures in the Astronomical Image Processing System (AIPS).

Our new observations included some new expanded VLA (EVLA) antennas and the observations were made in a spectral line (4-channel pseudo-continuum) mode, which resulted in a total effective bandwidth of $(2 \times 21.875 =) 43.75 \text{ MHz}$. Four ≈ 9 minute scans of each source were interspersed with 1 minute scans of a suitable phase calibrator. 0713+438 was used as the bandpass calibrator for the experiment. After the initial amplitude and phase calibration, AIPS tasks CALIB and IMAGR were used iteratively to self-calibrate (Schwab 1980) and image the sources. The resultant *rms* noise in the maps was typically of the order of $0.06 \text{ mJy beam}^{-1}$. The quasar 1124–186 was observed with an incorrect source position,

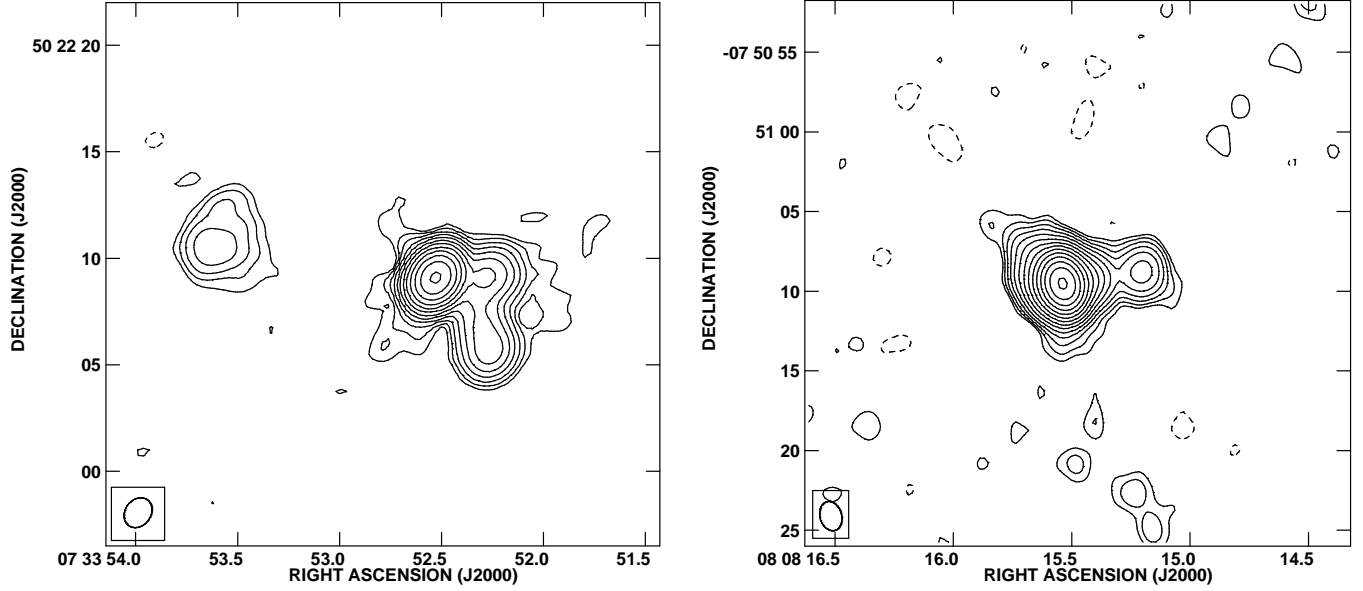


Fig. 1.— 1.4 GHz VLA images of the quasars 0730+504 (Left) and 0805–077 (Right). The contours are in percentage of the peak surface brightness and increase in steps of 2. The lowest contour levels and peak surface brightness are (Left) ± 0.042 , $672 \text{ mJy beam}^{-1}$ and (Right) ± 0.010 , $1.43 \text{ Jy beam}^{-1}$.

which resulted in significant beam smearing. We instead obtained archival VLA data for this source. The new radio images of the six sources are presented in Figures 1, 2, and 3.

Since most of the MOJAVE sources have highly compact radio structures, most of the archival data comprised of snapshot observations where the sample sources were observed as phase calibrators. By choosing archival datasets with exposure times $\gtrsim 10$ minutes, we were able to obtain maps with typical *rms* noise levels of $\sim 0.15 \text{ mJy beam}^{-1}$. We present previously unpublished images of 21 blazars in Appendix A.

A compilation of the basic parameters for each source is given in Table 1. The integrated flux densities for the cores were obtained in AIPS using the Gaussian-fitting task JMFIT, while the total flux densities were obtained by putting a box around the source, using the AIPS verbs TVWINDOW and IMSTAT. The extended radio flux density was obtained by subtracting the core flux density from the total radio flux density.

All the maps were created with uniform weighting using a ROBUST parameter of 0 in the AIPS task IMAGR. We also obtained core and lobe flux densities from maps with different weighting schemes (by using ROBUST parameters -5 and $+5$, respectively) for a fraction of the sample. We found that the integrated core flux density estimates differed typically by

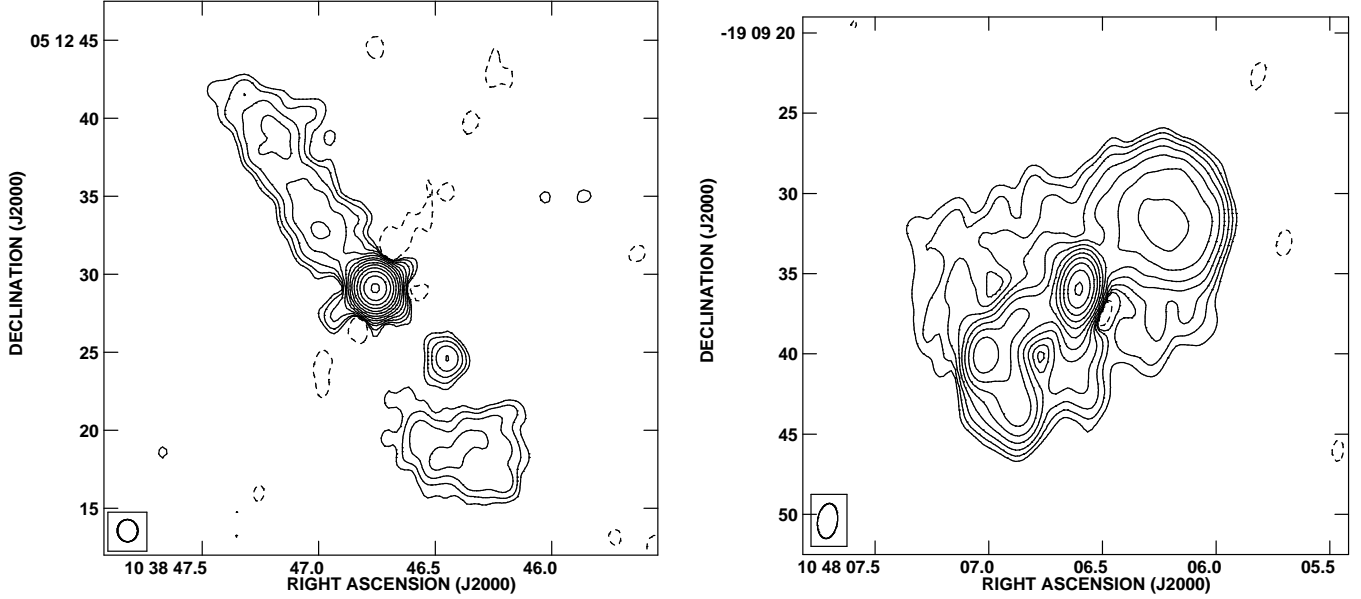


Fig. 2.— 1.4 GHz VLA images of 1036+054 (Left) and 1045–188 (Right). The contours are in percentage of the peak surface brightness and increase in steps of 2. The lowest contour levels and peak surface brightness are (Left) ± 0.021 , 892 mJy beam $^{-1}$ and (Right) ± 0.042 , 724 mJy beam $^{-1}$.

less than 1%, between different weighting schemes. The extended flux density values differed typically by < 2%, with a large majority of sources showing less than a 5% difference. Only in a handful of sources, where there seemed to be an unresolved compact component close to the core (e.g., 1038+064, 1417+385), was the difference between different weighting schemes significant (10%–20%). However, following our radio galaxy study (Kharb et al. 2008b), we have found that nearly 15%–20% of the extended flux density could be getting lost in A-array observations, compared to combined-array observations. Therefore, we conclude that the lack of short spacings in the A-array observations is far more detrimental to the determination of accurate extended flux values than (not) adopting different weighting schemes on the A-array data to obtain core and extended flux densities. The weighting scheme approach does suggest that the errors in the extended flux density values are typically of the order of 2%–5%, but could be of the order of 10%–20% for sources where a compact component close to the core is not clearly resolved.

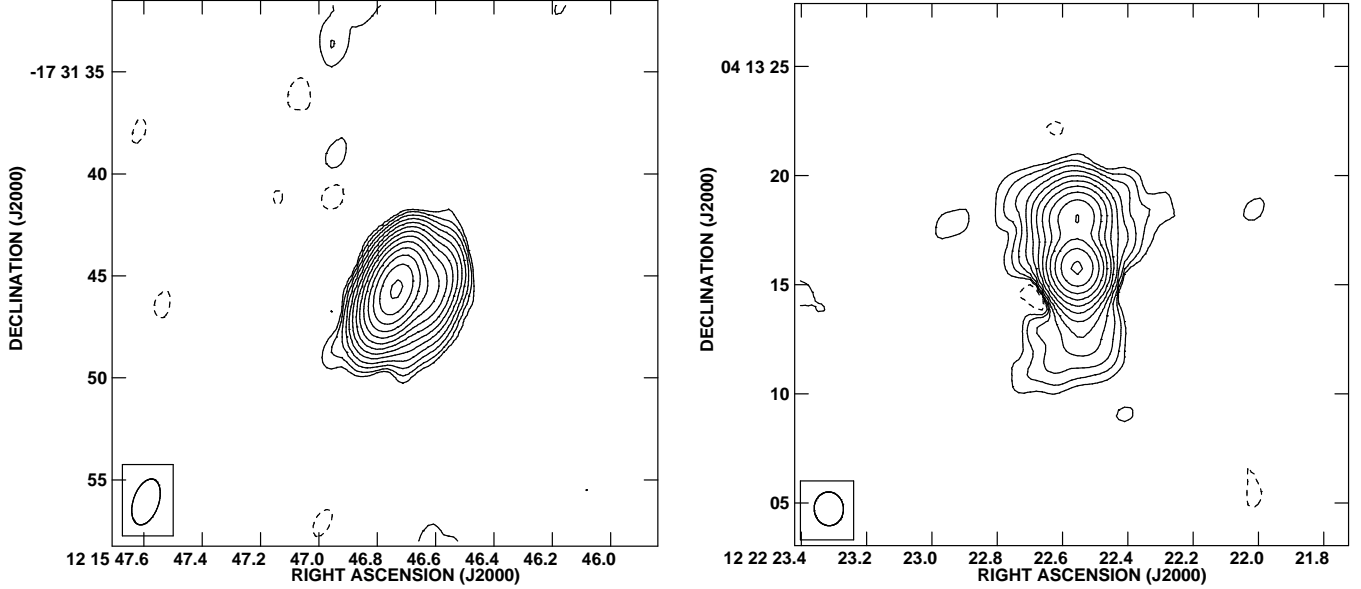


Fig. 3.— 1.4 GHz VLA images of 1213–172 (Left) and 1219+044 (Right). The contours are in percentage of the peak surface brightness and increase in steps of 2. The lowest contour levels and peak surface brightness are (Left) ± 0.021 , $1.66 \text{ Jy beam}^{-1}$ and (Right) ± 0.042 , $549 \text{ mJy beam}^{-1}$.

3. RESULTS

3.1. Extended Radio Power

The 1.4 GHz extended radio luminosities for the MOJAVE sources are plotted against redshift in Figure 4. Sources with no discernible extended emission are represented as upper limits. The solid lines indicate the FRI–FRII divide (extrapolated from 178 MHz to 1.4 GHz assuming a spectral index, $\alpha = 0.8$), following Ledlow & Owen (1996) and Landt et al. (2006). The right hand panel of Figure 4 demonstrates the close relation between the radio core and extended luminosity (Table 2). Using the partial correlation regression analysis routine in IDL (P_CORRELATE), we found that the linear correlation between $\log L_{\text{core}}$ and $\log L_{\text{ext}}$ is strong even with the effects of luminosity distance ($\log D_L$) removed (partial correlation coefficient, $r_{XYZ} = 0.303$, t statistic = 3.41, two-tailed probability that the variables are not correlated³, $p = 0.0009$). We note that the 18 BL Lacs (ones with redshift information) alone fail to show a correlation between $\log L_{\text{core}}$ and $\log L_{\text{ext}}$, when the effects of luminosity distance are removed. The implication of this finding is discussed ahead in

³Calculated using the VassarStats statistical computation website, <http://faculty.vassar.edu/lowry/VassarStats.html>

§3.3.

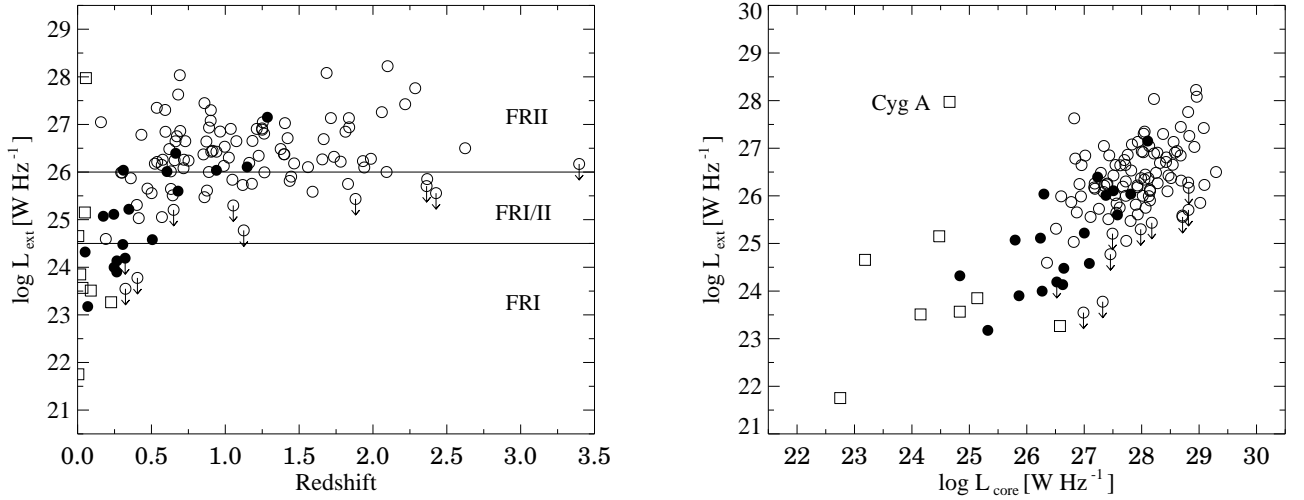


Fig. 4.— (Left) 1.4 GHz extended luminosity versus redshift. (Right) 1.4 GHz core versus extended luminosity. Open and filled circles denote quasars and BL Lacs, respectively, while open squares denote radio galaxies. Core-only sources are represented as upper limits.

The salient features of the extended radio emission in the MOJAVE blazars are:

- (i) Six of the 22 BL Lacs ($\sim 27\%$) have FRII radio powers ($\log L_{ext}^{1.4} > 26$). Four of these (*viz.*, 0235+164, 0716+714, 0808+019, 2131−021) also have hot spots like quasars.
- (ii) Five BL Lacs ($\sim 23\%$) fall in the FRI/II power range ($24.5 < \log L_{ext}^{1.4} < 26$). Two of these (*viz.*, 0823+033, 1803+784) also appear to have hot spots.
- (iii) Seven BL Lacs have extended luminosity $\log L_{ext}^{1.4} < 24.5$ and could be regarded as the true beamed counterparts of FRI radio galaxies. However, three of these (*viz.*, 0754+100, 0851+202, 1807+698) also appear to exhibit hot spot-like features. Hot spots may also be present in all four BL Lacs with no redshift information. Overall, nearly 60% of the MOJAVE BL Lacs appear to have hot spots. The hot spots in some BL Lacs are however not as bright or compact as those observed in quasars.
- (iv) Excluding the upper limits, 22 quasars ($\sim 22\%$) fall in the FRI/II power range.
- (v) 10 sources ($\sim 7\%$, 9 quasars, 1 BL Lac) do not show any extended emission – these are discussed in §3.4.

Based on the extended emission at 1.4 GHz, we can conclude that a substantial fraction of the MOJAVE BL Lacs have both radio powers and radio morphologies like FRIIs or quasars. A substantial fraction of the MOJAVE quasars lie in the intermediate (FRI/II) luminosity range. These results are consistent with a number of previous radio studies. Using a large sample of radio core-dominated AGNs, Murphy et al. (1993) observed that many high redshift ($z > 0.5$) BL Lacs lie above the FRI/FRII luminosity division. Using a sample of 17 BL Lacs, mostly belonging to the 1-Jy sample, Kollgaard et al. (1992) suggested that about 12% – 30% of BL Lacs in a radio flux-limited sample may be bona fide FRIIs. Based on extended radio emission and strong emission lines at one or more epochs, Rector & Stocke (2001) concluded that many radio-selected BL Lacs belonging to the 1 Jy sample (Stickel et al. 1991) cannot be beamed FRIs, but are more likely to be beamed FRIIs. Cara & Lister (2008) found similar intrinsic parent luminosity functions for the MOJAVE sample (consistent with FRIIs) irrespective of whether the BL Lacs were included or not.

3.2. Radio Morphology

We observe from Figures 1–3 that all but two sources show two-sided radio structures. The variety of radio structures observed here are reasonably representative of the entire sample (e.g., see Cooper et al. 2007), as well as those previously observed in other quasar surveys (e.g., Gower & Hutchings 1984; Antonucci & Ulvestad 1985; Pearson & Readhead 1988; Murphy et al. 1993). The quasars often show two-sided radio structures with hot spots on one or both sides of the core. However, one-sided morphologies with no discernable compact or diffuse emission on the other side of the core, are also common.

While determining if the blazars had an FRII type radio morphology, we relied initially on the presence of one or more compact hot spots at the leading edge of the radio lobes. When no clear hot spots were visible on either side of the cores, we resorted to the traditional “edge-brightened” definition for FRII sources, *i.e.*, when the brightest radio emission was furthest from the core, we classified the source as an FRII. The remaining sources with no clear hot spots, and the brightest extended emission closest to the cores, were classified as FRI types. Even then, it was sometimes difficult to consign the sources to FRI or FRII classes, and we have listed more than one morphology for some sources in Table 1.

Many of the MOJAVE sources show distinctly curved kiloparsec-scale jets. Straight jets are a rarity in the sample. Many MOJAVE quasars exhibit large parsec-to-kiloparsec jet misalignments. While any intrinsic curvature in the jets is likely to be highly exaggerated by projection effects in these low-viewing angle blazars, many sources seem intrinsically distorted. We discuss in §4.1 how the MOJAVE selection criteria might be preferentially

picking up bent jets. Apart from highly curved jets, many sources show distinct hot spot-like features both closer to the core and at the jet termination points, similar to the wide angle tail (WAT) radio galaxies (e.g., O'Donoghue et al. 1990).

Four MOJAVE blazars have not yet been identified as quasars or BL Lacs (Table 1). A new VLA image of one of the unidentified sources (*viz.*, 1213–172) is presented in Figure 3. Another unidentified source (0648–165) has a similar core-dominant radio morphology (Cooper et al. 2007). A third source (2021+317) has a distinct core-halo morphology resembling a BL Lac object (see Appendix A), while the fourth (0446+112) has a straight jet with a possible hot spot at the end (Cooper et al. 2007).

3.3. Parsec-scale Jet Speeds and Extended Luminosity

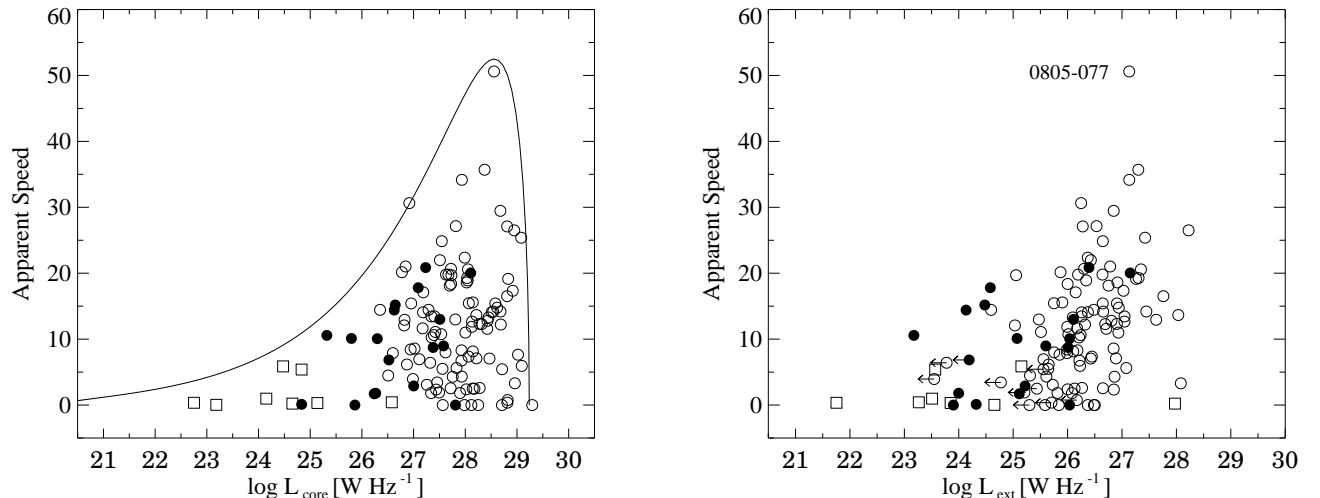


Fig. 5.— (Left) 1.4 GHz core luminosity versus the apparent jet speed. The aspect curve assumes $\gamma = 52$, $L_{\text{int}} = 5 \times 10^{24}$ and $p \approx 2$. (Right) 1.4 GHz extended luminosity versus the apparent jet speed. Open and filled circles denote quasars and BL Lacs, respectively, while open squares denote radio galaxies. Core-only sources are represented as upper limits.

The MOJAVE and 2 cm survey programs have provided apparent parsec-scale jet speeds (β_{app}) for nearly the entire MOJAVE sample, by monitoring structural changes over timescales of approximately a decade. These have been previously tabulated by Kellermann et al. (2004), and most recently by Lister et al. (2009b). For our analysis below, we use a β_{app} value that represents the fastest moving feature in that source.

The parsec-scale apparent jet speeds and kiloparsec-scale radio core luminosity (Fig. 5)

are related by standard beaming relations. The aspect curve in Figure 5 assumes: $L = L_{int} \times \delta^p$, $\beta_{app} = \beta \sin \theta / (1 - \beta \cos \theta)$, where the Doppler factor, $\delta = 1 / (\gamma (1 - \beta \cos \theta))$ and $\beta = v/c$. The best-fit values for the curve are $\gamma = 52$, $L_{int} = 5 \times 10^{24}$ and $p \approx 2$. The relation between parsec-scale apparent jet speeds and parsec-scale core luminosity for the MOJAVE sample is discussed in greater detail by Cohen et al. (2007), and Lister et al. (2009b).

We find that the parsec-scale apparent jet speeds are correlated significantly with the extended radio luminosity (Fig. 5, Table 2). Partial regression analysis shows that the linear correlation between $\log L_{ext}$ and β_{app} with the effects of luminosity distance removed, is still highly significant ($r_{XYZ} = 0.273$, t statistic = 3.05, two-tailed probability, $p = 0.0028$). This implies that more radio powerful sources have faster radio jets. Since extended radio luminosity is correlated with the core luminosity (Fig. 4, Table 2), and the core luminosity is related to the apparent jet speed, we tested the correlation with a partial correlation test between extended radio luminosity and apparent jet speeds, after removing the effects of radio core luminosity. This too yielded a statistically significant correlation between extended radio luminosity and parsec-scale apparent jet speeds ($r_{XYZ} = 0.246$, t statistic = 2.72, $p = 0.0075$).

The significant implication of this result is that faster jets are launched in AGNs with larger kiloparsec-scale lobe luminosities. It would therefore appear that the fate of the AGN is decided at its conception. This result undermines the role of the kiloparsec environment on the radio power of a given source. It also indicates that the 1.4 GHz extended emission is indeed related to jet kinetic power, contrary to some suggestions in the literature (e.g., Bîrzan et al. 2004). Given that there is a large overlap in radio powers between quasars and BL Lac objects, it can be concluded that most quasars have faster jets than most BL Lac objects.

The second noteworthy inference that can be drawn from Figure 5 is that there is a continuous distribution of parsec-scale jet speeds going from BL Lacs to quasars. This supports the idea that the distinction between the BL Lac and quasar population, at an equivalent width of 5\AA , is essentially an arbitrary one at least in terms of radio jet properties (see also Scarpa & Falomo 1997).

However, we note that inspite of the two blazar classes displaying a smooth continuation in properties (as is evident in Fig. 5 and other plots), they sometimes reveal differences in the correlation test results when considered separately. In Table 2 we have listed the correlation test results separately for quasars and BL Lacs, if they differed from results for the combined blazar population. BL Lacs considered alone sometimes failed to exhibit the correlations observed in quasars (also see §3.1). Apart from the possible effects of small number statistics, a simple interpretation of this finding could be that unlike the quasars,

the BL Lacs do not constitute a homogeneous population. As has been previously suggested in the literature (e.g., Owen et al. 1996; Cara & Lister 2008; Landt & Bignall 2008), the BL Lacs might constitute the beamed population of both FRI and FRII radio galaxies. We note that Giroletti et al. (2004) have demonstrated that HBLs (which are absent in MOJAVE) conform to the standard unification scheme with respect to FRI radio galaxies. This again supports the proposed inhomogeneity within the BL Lac class.

Preliminary Monte Carlo simulations of a population of AGN similar to that of MOJAVE also show a correlation between apparent jet speed and extended luminosity (Cooper et al., in preparation). The simulations are based on the luminosity function of Padovani & Urry (1992), and assume that the extended luminosity is unbeamed and proportional to the intrinsic unbeamed parsec-scale luminosity. We are currently incorporating the luminosity function derived from the MOJAVE sample by Cara & Lister (2008) into the simulations.

3.4. Parsec-to-kiloparsec Jet Misalignment

Apparent misalignment in the jet direction from parsec to kiloparsec scales is commonly observed in blazars (e.g., Pearson & Readhead 1988). This misalignment could either be due to actual large bends in the jets, or due to small bends that are amplified by projection. We present the parsec- to kiloparsec-scale jet misalignment for the MOJAVE sources in Figure 6. The procedure for estimating the parsec-scale jet position angles (PAs) is described in Lister et al. (2009a). Kiloparsec-scale jet position angles were determined for the FRII sources using the brightest hot spots, especially when no jet was clearly visible, under the assumption that the brightest hot spot indicates the approaching jet direction due to Doppler boosting. The AIPS procedure TVMAXFIT was used to obtain accurate peak pixel positions of the core and hot spot, which were then used in the AIPS verb IMDIST to obtain the jet position angle. For the FRI-type sources we used TVMAXFIT for the core pixel position, and the AIPS verb CURVALUE to get the pixel position roughly towards the center and end of the broad jet/lobe. Finally IMDIST was used to obtain the jet position angle. Note that unlike regular radio galaxies, FRI blazars are typically one-sided, which makes the approaching jet direction easy to identify. Due to the wide jet/lobes in FRIs, the kiloparsec-scale jet position angle could be uncertain by 10° to 15° . When a jet feature appeared only partially resolved (*viz.*, 1038+064, 1417+385), a two Gaussian component model was used in JMFIT to obtain pixel positions of the core and jet feature.

We note that our approach (*viz.*, of using the brightest hot spot to determine the approaching jet direction, when no jet was clearly visible) differs from that adopted by some other authors (e.g., Xu et al. 1994) who assume that, when no jet is visible, the hot spot on

the side of the parsec-scale jet, represents the kiloparsec-scale jet direction. Our approach has led us to identify many more sources ($\sim 30\%$) with misalignment angles greater than 90° .

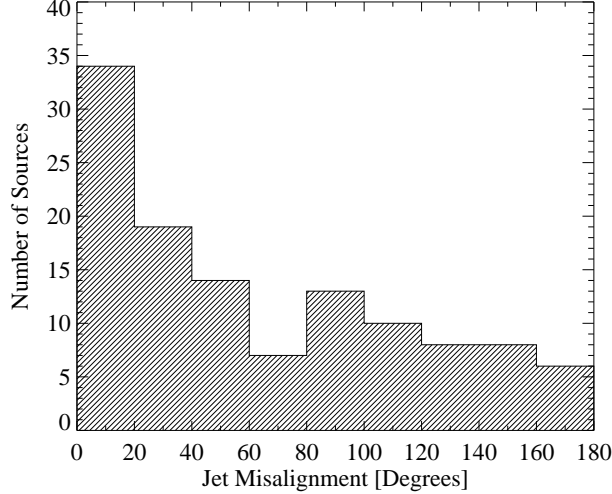


Fig. 6.— Misalignment angle between the parsec-scale and the kiloparsec-scale jet for the MOJAVE sources. There are signatures of a weak 90° bump.

For an otherwise straight jet having a single bend, the apparent bending angle (η) is related to the intrinsic bending angle (ψ) through the relation, $\cot \eta = \frac{\cot \psi \sin \theta - \cos \theta \cos \phi}{\sin \phi}$, where θ is the angle to line of sight, and ϕ is the azimuth of the bend (Appl et al. 1996). The fact that we see a majority of sources having close to zero apparent misalignment implies one of the following scenarios: (i) the intrinsic misalignment angle is small; (ii) both the intrinsic misalignment and jet inclination angles are large; (iii) the azimuth of the bend is close to 180° , *i.e.*, the plane of the bend is perpendicular to the sky plane. Since scenario (ii) is unlikely for these blazars, possibilities (i) and (iii) are more favorable. In §4, we explain how the MOJAVE selection criteria could make it biased towards bent jets.

Pearson & Readhead (1988) and Conway & Murphy (1993) reported an unexpected secondary peak at $\Delta PA = 90^\circ$ in the misalignment angle distribution. The signatures of a weak 90° bump appear to be present in Figure 6. Conway & Murphy (1993) concluded that while the largely aligned population could be explained by straight parsec-scale jets and small intrinsic bends between parsec- and kiloparsec-scales, the secondary peak sources must have gently curving (low-pitch) helical parsec-scale jets. This helical distortion could arise due to Kelvin-Helmholtz instabilities or precession of the jet ejection axes. We reach a similar conclusion on the jet misalignments, following a different approach in §4.3.

4. DISCUSSION

4.1. Selection Effects in MOJAVE

The MOJAVE survey appears to select many sources with intermediate radio powers and radio morphology (e.g., high radio power BL Lacs, some with hot spots, and low radio power quasars). This could be a result of the MOJAVE selection criteria, which are based on the relativistically-boosted, high radio frequency (15 GHz) parsec-scale flux densities. This would make it more likely to encompass a much larger range in intrinsic radio powers, compared to other samples selected on the basis of total kiloparsec-scale flux-densities (e.g., the 3CR sample). The intrinsic radio luminosity function derived for the MOJAVE sample by Cara & Lister (2008) also supports this view.

Furthermore, as the MOJAVE survey picks up bright radio cores, most of the sources could either be fast jets pointed towards us, or curved/bent jets that have at least some portion of the jet aligned directly into our line of sight, at at least one epoch (e.g., Alberdi et al. 1993). The MOJAVE survey could therefore be biased towards bent jets. Note that in the wide angle tail quasars, the hot spots closer to the cores could be produced at the base of the plumes (e.g., Hardcastle & Sakelliou 2004), or indicate a sharp bend in the jet (e.g., Alberdi et al. 1993; Jetha et al. 2006). We discuss the possibility of beamed WAT quasars in the MOJAVE sample further in §4.3.

4.2. Orientation Effects in the Sample

Since the MOJAVE sample consists almost entirely of blazars, the sources are expected to have jets aligned close to our line of sight. Our examination of orientation effects in the sample, however, using two different statistical orientation indicators, R_c and R_v , reveals that a range of orientations must in fact be present in order to account for several observed trends. R_c and R_v also reveal, to some extent, dissimilar trends. We finally reach the conclusion that R_v is a better indicator of orientation for this blazar sample.

The ratio of the beamed radio core flux density (S_{core}) to the unbeamed extended radio flux density (S_{ext}), *viz.*, the radio core prominence parameter (R_c), has routinely been used as a statistical indicator of Doppler beaming and thereby orientation (Orr & Browne 1982; Kapahi & Saikia 1982; Kharb & Shastri 2004). The k -corrected R_c ($= \frac{S_{core}}{S_{ext}}(1+z)^{\alpha_{core}-\alpha_{ext}}$, with $\alpha_{core} = 0$, $\alpha_{ext} = 0.8$) is plotted against the radio core luminosity in Figure 7. As expected, R_c is correlated with the radio core luminosity (Table 2). R_c however, shows a significant anti-correlation with respect to the extended radio luminosity (Fig. 8). R_c does

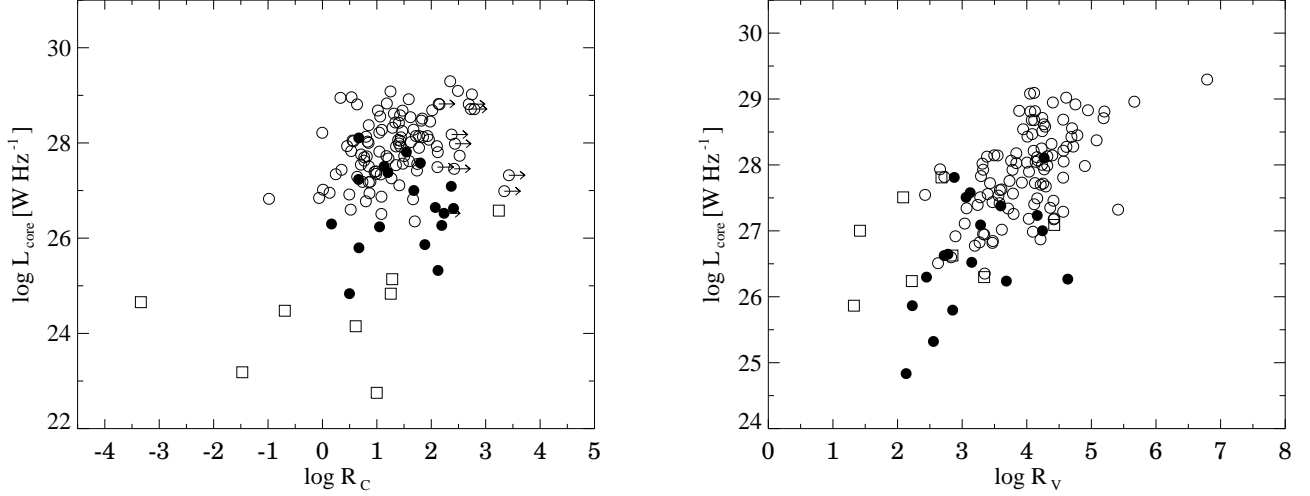


Fig. 7.— The orientation indicators, R_c (Left) and R_v (Right) versus the 1.4 GHz core luminosity. Open and filled circles denote quasars and BL Lacs, respectively, while open squares denote radio galaxies. Core-only sources are represented as upper limits.

not show a correlation with jet misalignment (Table 2). In fact the quasars considered alone showed a weak anti-correlation between R_c and jet misalignment (implying that the more core-dominant sources have smaller jet misalignments). These results are unexpected, because in the former case, the extended radio luminosity is expected to be largely unbeamed, while in the latter, the jet misalignment is affected by projection and therefore orientation (in the sense that the more core-dominant sources show larger jet misalignments, e.g., Kapahi & Saikia 1982). As an aside, Brotherton (1996) have noted that the anti-correlation between $\log R_c - \log L_{ext}$ may be suggesting that core-dominated quasars are intrinsically fainter than their lobe-dominated counterparts. This would be consistent with the idea that the MOJAVE sources span a large range in intrinsic radio powers (*cf.* §4.1).

We also examined the relationship between R_c and apparent jet speed. While both R_c and β_{app} depend on the Lorentz factor and orientation, many of the viewing angles may be inside the critical angle for maximum superluminal speed, which would spoil any correlation. However, the quasars considered alone do show a significant anti-correlation, contrary to expectations. But as we see below, the alternate orientation indicator, R_v , does show the expected behavior.

Wills & Brotherton (1995) defined R_v as the ratio of the radio core luminosity to the k -corrected absolute V-band magnitude (M_{abs}): $\log R_v = \log \frac{L_{core}}{L_{opt}} = (\log L_{core} + M_{abs}/2.5) - 13.7$, where $M_{abs} = M_V - k$, and the k -correction is, $k = -2.5 \log (1+z)^{1-\alpha_{opt}}$ with the optical

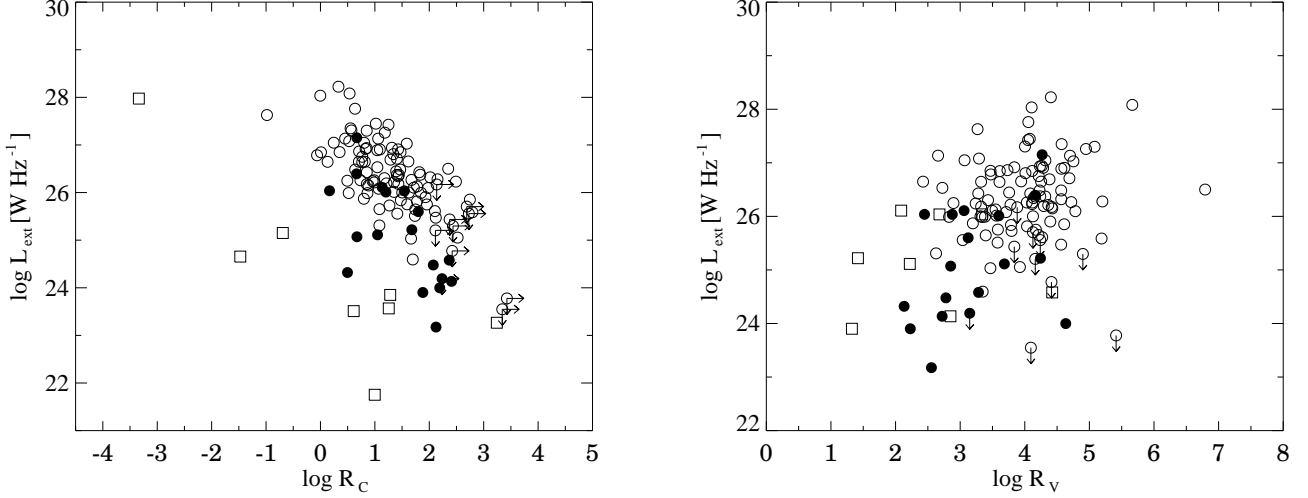


Fig. 8.— The orientation indicators, R_c (Left) and R_v (Right) versus the 1.4 GHz extended luminosity. Open and filled circles denote quasars and BL Lacs, respectively, while open squares denote radio galaxies. Core-only sources are represented as upper limits.

spectral index, $\alpha_{opt} = 0.5$. R_v is suggested to be a better orientation indicator than R_c since the optical luminosity is likely to be a better measure of intrinsic jet power (e.g., Maraschi et al. 2008; Ghisellini et al. 2009) than extended radio luminosity. This is due to the fact that the optical continuum luminosity is correlated with the emission-line luminosity over four orders of magnitude (Yee & Oke 1978), and the emission-line luminosity is tightly correlated with the total jet kinetic power (Rawlings & Saunders 1991). The extended radio luminosity, on the other hand, is suggested to be affected by interaction with the environment on kiloparsec-scales.

Figure 7 suggests that R_v is indeed a better indicator of orientation as the correlation with radio core luminosity gains in prominence (see Table 2). R_v shows a weak positive correlation with the extended radio luminosity (Fig. 8). Partial regression analysis however, shows that the linear correlation between $\log R_v$ and $\log L_{ext}$ is no longer significant when the effects of $\log L_{core}$ are removed ($r_{XYZ} = 0.078$, t statistic = 0.84, $p = 0.4013$). This implies that the extended radio emission is largely unbeamed. R_v is correlated with the parsec-to-kiloparsec jet misalignment, suggesting that orientation does play a role in the observed jet misalignments, at least for the quasars. The lack of such a correlation for the BL Lacs could again be interpreted to be consequence of their comprising of not only beamed FRIIs (which could have intrinsically distorted jets) but beamed FRIIs as well. We discuss this point again in §4.5. Finally, there appears to be no correlation between R_v and β_{app} , as is expected if many blazar viewing angles are inside the critical angle for maximum superluminal speeds,

which would then result in smaller apparent speeds. This result is again consistent with R_v being a better indicator of orientation than R_c .

Here we would like to note that the correlation between apparent jet speed and absolute optical magnitude does not seem to be as significant as the one observed between apparent jet speed and extended radio luminosity (Table 2). This could in principle undermine the suggestion that the optical luminosity is a better indicator of jet kinetic power than extended radio luminosity. However, since the optical luminosity is more likely to be affected by strong variability, than the extended radio luminosity, the lack of a strong correlation can perhaps be accounted for, in these non-contemporaneous radio and optical observations. Nevertheless, this is an important result to bear in mind, that requires further testing.

4.3. Environmental Effects

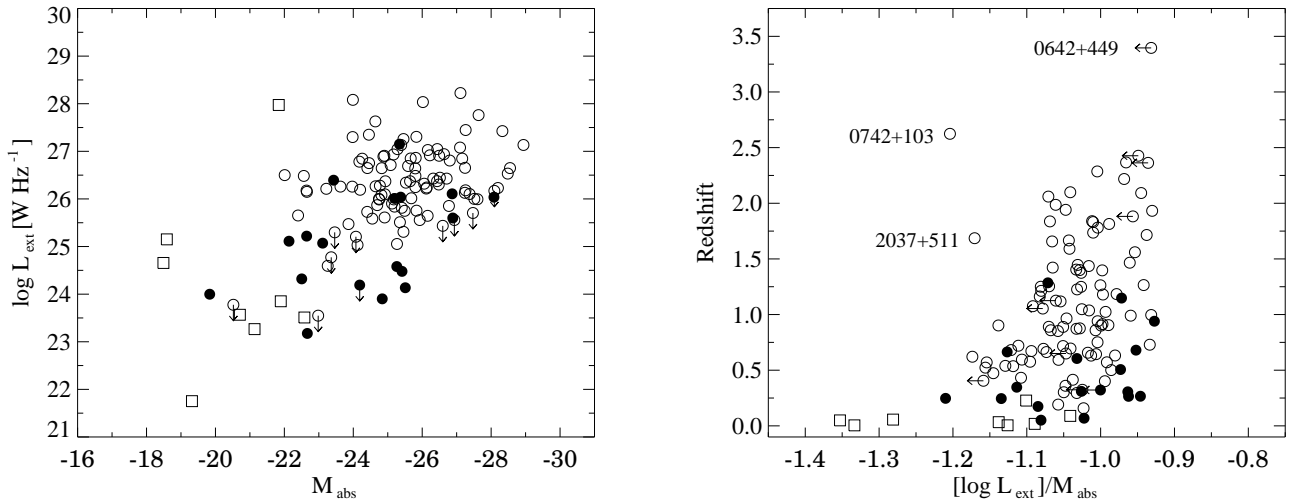


Fig. 9.— (Left) 1.4 GHz extended radio luminosity versus the absolute optical magnitude. (Right) The environment indicator versus redshift. Open and filled circles denote quasars and BL Lacs, respectively, while open squares denote radio galaxies. Core-only sources are represented as upper limits.

It has been suggested that apart from projection and relativistic beaming effects, the complex radio structures in quasars could arise due to interactions with the surrounding medium (Pearson & Readhead 1988; Barthel & Miley 1988). As is observed in Figure 9, the extended radio luminosity appears to be correlated with absolute optical luminosity. However, a partial regression analysis shows that the linear correlation becomes weak or non-

existent, after the effects of luminosity distance are removed (for quasars, $r_{XY.Z} = -0.169$, t statistic = -1.62 , $p = 0.1088$; for BL Lacs, $r_{XY.Z} = 0.079$, t statistic = 0.31 , $p = 0.7608$). The lack of a strong correlation may again be attributable to strong optical variability in these blazars. If the extended radio luminosity is indeed affected by interaction with the kiloparsec-scale environment, and the optical luminosity is closely related to the AGN power, the ratio $[\log L_{ext}]/M_{abs}$, can serve as a probe for environmental effects on kiloparsec-scales (as suggested by Wills & Brotherton 1995). Henceforth we will refer to this ratio as the “environment indicator” (we will drop the “log” term in the ratio for convenience, in the following text).

A higher value of the ratio could indicate greater jet-medium interaction, (as say, from an asymmetrically dense source environment). Dense environments can decrease expansion losses in the source, but increase radiative losses, making the sources brighter at low radio frequencies (e.g., in Cygnus A, see Barthel & Arnaud 1996). Note that the optical magnitude in blazars is expected to be related to the AGN (accretion disk or jet), rather than to starlight. This might not be true for the nearby radio galaxies, where starlight might indeed be a significant contributor to the optical magnitude. The L_{ext}/M_{abs} ratio might therefore not be a good environment proxy for the radio galaxies. We have therefore excluded radio galaxies from the correlation tests related to the environment proxy indicator.

We plot the environment proxy ratio with respect to redshift in the right hand panel of Figure 9 and find a strong positive correlation. The “alignment effect” between the radio source axis and the emission line region in high redshift radio *sources* demonstrates that local galactic asymmetries (on scales of several kiloparsecs) increase with redshift (McCarthy 1993; Best et al. 1999). This result therefore, is consistent with the suggestion of the environmental dependence of the extended luminosity. We note that the BL Lacs considered alone fail to show a strong correlation (Table 2), which could be a consequence of an inhomogeneous parent population, as discussed in §3.3.

We find that while the parsec-scale jet speeds appear to be tightly correlated with the extended radio luminosity (Fig. 5), and weakly correlated with the optical luminosity, they seem to not show any correlation with the kpc-scale environment indicator (Fig. 10). This could imply that the parsec-scale jet speeds are not driven by the kiloparsec-scale environment, but rather by factors intrinsic to the AGN, or the AGN’s local parsec-scale environment. For instance, the jet speeds could be related to the black hole spins (e.g., Meier 1999). However, like other results pertaining to optical luminosity, this lack of a correlation needs further testing with contemporaneous optical and radio data.

We find that the parsec-to-kiloparsec jet misalignment is not correlated with redshift (Fig. 11). This goes against the idea that the bending of the jets is influenced by interaction

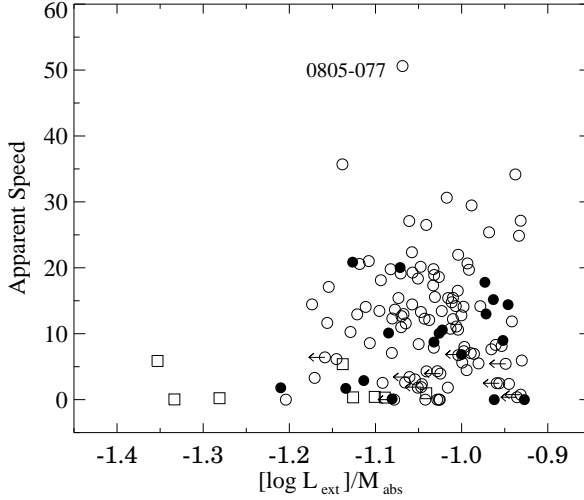


Fig. 10.— Apparent parsec-scale jet speed versus the environment indicator. Open and filled circles denote quasars and BL Lacs, respectively, while open squares denote radio galaxies.

with the medium; an effect which should get more prominent with increasing redshift. This result is consistent with the suggestions of Hintzen et al. (1983) and Appl et al. (1996). We note that Hintzen et al. (1983) used the kiloparsec-scale jet-to-counterjet misalignment in their study. Kharb et al. (2008b) found a similar lack of correlation between jet-to-counterjet misalignment and redshift for an FRII radio galaxy sample. Thus, the jet misalignment could also be related to factors closely associated with the AGN itself. For instance, the presence of binary black holes or kicks imparted to the black hole via a black hole merger, could switch the ejection direction on a short timescale (e.g., Begelman et al. 1980; Merritt & Ekers 2002). Black hole re-alignment due to a warped accretion disk could also give rise to jet precession (Pringle 1997). We note that a few sources have morphologies resembling fast, precessing jets (“banana” shaped) as modelled by Gower et al. (1982). Alternatively, the jet misalignment could be influenced by the AGN’s local parsec-scale environment.

The jet misalignment is inversely correlated with the kpc-scale environment indicator (see right hand panel of Fig. 11). The inverse relation suggests that jets with smaller misalignments (*i.e.*, straighter jets) show signatures of greater environmental effects on their lobe emission. This could either be suggestive of a uniformly dense confining medium on different spatial scales around the source, or, of projection effects in the sample, which could boost the optical emission and decrease the $L_{\text{ext}}/M_{\text{abs}}$ ratio in sources with larger jet misalignments. If the latter is true, then this is an important caveat — the environment indicator could also be affected by source orientation in blazars. However, the orientation-dependence alone

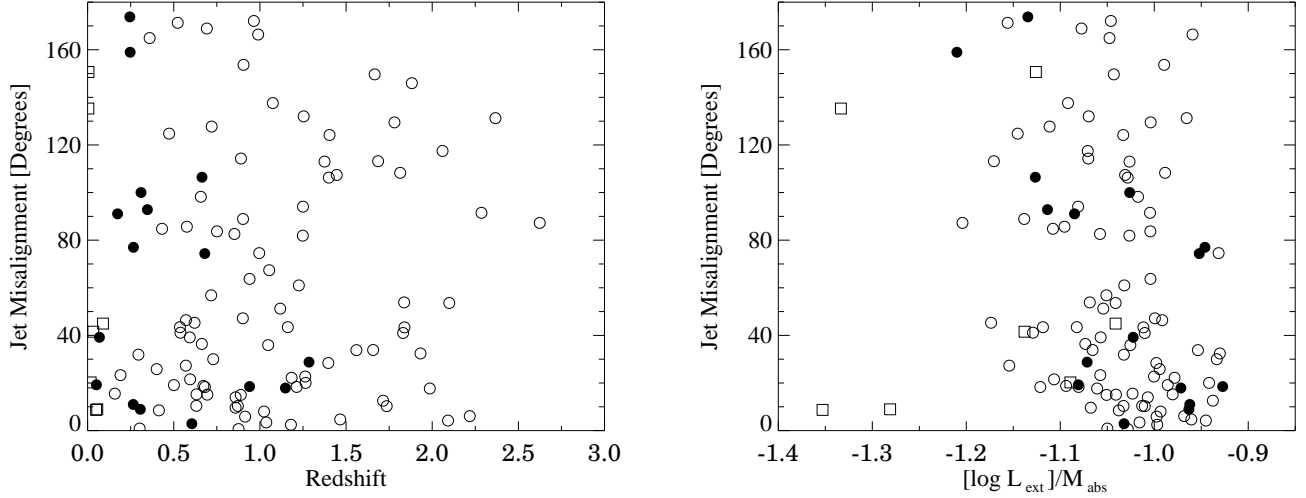


Fig. 11.— (Left) Jet misalignment versus the environment indicator. (Right) Misalignment angle versus redshift. Open and filled circles denote quasars and BL Lacs, respectively, while open squares denote radio galaxies.

cannot satisfactorily explain the correlation between the environment indicator and redshift (Fig. 9).

Many MOJAVE blazars exhibit radio structures resembling those of *wide angle tail* radio galaxies. Observations have indicated that WAT quasars could be members of rich galaxy clusters (e.g., Hintzen et al. 1983; Harris et al. 1983; Blanton et al. 2000). Using the NASA/IPAC extragalactic database (NED) we found that nearly 7% of the MOJAVE sources have a galaxy cluster $\sim 5'$ away, while 14% have a galaxy cluster $\sim 10' - 15'$ away. While this fraction appears to be small, we must keep in mind that most of the blazars are at high redshifts, while the cluster information is highly incomplete even at redshifts $z > 0.1$ (e.g., Ebeling et al. 1998; Böhringer et al. 2004). Thus the possibility remains that a large number of MOJAVE blazars inhabit galaxy clusters. This suggestion has interesting ramifications, as discussed below. Furthermore, this could help us understand some of the results discussed in this section.

4.4. Relation Between Radio Power and Emission-line Luminosity

Rawlings & Saunders (1991) demonstrated a tight correlation between emission-line luminosity and total jet kinetic power in a sample of radio-loud AGNs. This correlation was tighter than the one observed between emission-line luminosity and radio luminosity.

Landt et al. (2006) discovered a large number of “blue quasars” with strong emission lines, but relatively low radio powers in the Deep X-ray Radio Blazar Survey (DXRBS) and the RGB samples, and suggested that this went against the close relationship between emission-line and jet power. These and other observations (e.g., Xu et al. 1999) could be suggesting that the mechanism for the production of the optical-UV photons that ionise the emission-line clouds is decoupled from the mechanism that produces powerful radio jets. Many MOJAVE blazars also seem to not follow the relation between emission-line and radio luminosity; that is, some quasars and BL Lacs have relatively low and high radio powers, respectively, and the suggestion of decoupled mechanisms might hold true. However, an alternate hypothesis by which their emission-line luminosity could still be correlated with their intrinsic jet kinetic power, could come about if the outlying BL Lac objects were present in dense confining environments, while the outlying quasars were old, field sources. Confinement would increase the synchrotron radiative losses due to the amplification of the magnetic field strength, making the sources brighter (see Barthel & Arnaud 1996), while expansion losses and gradual radiative losses could presumably reduce the low frequency radio emission in the old, field quasars.

It has been suggested that a large fraction ($\sim 50\%$) of the high redshift radio sources could be GPS sources (e.g., O’Dea et al. 1991), which are likely to be present in confined environments. One of the highest redshift MOJAVE sources, 0742+103 ($z = 2.624$), is a GPS quasar. There are several other MOJAVE sources that have peaked spectra, but do not show the low-variability or the double-lobed parsec-scale structures that are characteristic of the GPS class. These could be “masquerading GPS” sources, whose overall spectrum happens to be dominated by an unusually bright feature in the jet, located downstream from the core.

4.5. Blazar Division Based on Radio Power

In order to gain more insight into the primary factors that drive the FR dichotomy, in this section we disregard the emission-line division (i.e., quasars, BL Lacs), and divide sources into FRI, FRI/II and FRII classes based solely on their 1.4 GHz extended powers (following Fig. 4). Figure 12 plots the environment indicator, L_{ext}/M_{abs} , with respect to redshift, using the new classification. A quick comparison with Fig. 9 reveals that many of the low redshift quasars fall into the intermediate FRI/II class. The low redshifts of these sources discounts the possibility of a $(1 + z)^4$ surface brightness dimming effect in them, which could potentially reduce their extended luminosity, making them fall in the intermediate luminosity class. This finding is consistent with the discovery of “blue quasars”

by Landt et al. (2006), which have radio powers and spectral energy distributions (SEDs) similar to the high energy peaked BL Lacs.

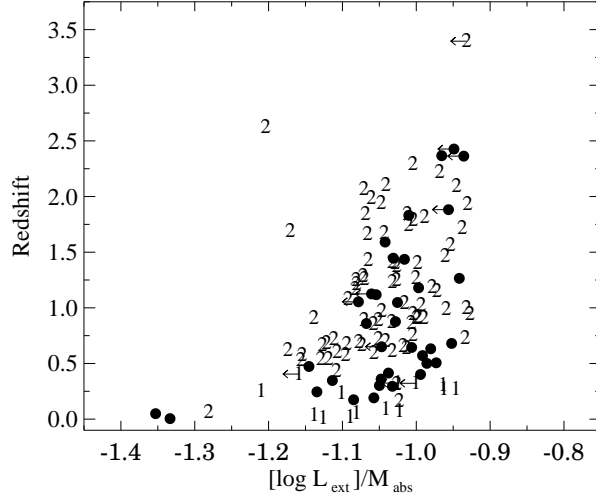


Fig. 12.— The environment indicator versus redshift, with sources divided on the basis of extended radio luminosity into FRI (=1), FRII (=2), and FRI/II (=filled circles).

Most beamed FRIs lie at redshifts below 0.5 in Fig. 12. This could be a limitation of the flux limited sample. Interestingly, the FRI/II sources lie at all redshift ranges, and throughout the L_{ext}/M_{abs} distribution. This suggests that these “intermediate” luminosity sources are not produced as a result of different environmental conditions compared to, say, other FRIIs. Similarly, sources divided on the basis of the presence or absence of hot spots, show no discernable difference in the L_{ext}/M_{abs} vs. z plane. It is important to note that environmental radio boosting, as mentioned in §4.4 (also Barthel & Arnaud 1996) could be instrumental in blurring the Fanaroff-Riley dividing line in the MOJAVE blazars.

Lastly, the orientation indicator, R_v , seems to be correlated with misalignment only for FRIIs, but not for FRIs or FRI/IIs (Table 2). This implies that projection is playing a significant role in the jet misalignment of FRII sources, but the jets are intrinsically more distorted in FRIs and FRI/IIs. A corollary to this is that the differences between FRIs and FRIIs could be related to factors affecting the black hole spin direction, since we have previously concluded that jet misalignments appear to be largely unrelated to kiloparsec-scale environmental effects.

4.6. Extremely Misaligned Sources

Six MOJAVE sources (*viz.*, 0224+671, 0814+425, 1219+044, 1510–089, 1828+487, 2145+067) have jet misalignments greater than 160° . Such extremely misaligned sources could be bent jets viewed nearly head-on, as suggested for the gamma-ray blazar PKS 1510–089 (Homan et al. 2002). An alternate scenario could be that some of these misaligned sources are “hybrid” morphology sources (e.g., Gopal-Krishna & Wiita 2000). Three of six sources with large misalignments (*viz.*, 0224+671, 1219+044, 1510–089) indeed seem to possess radio morphologies that could be classified as “hybrid”. The large misalignment then makes sense: the VLBI jet (used to determine the parsec-scale jet position angle) could be on the FRI side, while the sole hot spot (used to determine the kiloparsec-scale jet position angle) could be on the FRII side.

One interesting source that shows extreme misalignment ($\sim 135^\circ$) is M87 (1228+126). M87 appears to exhibit a weak hot spot on the counterjet side (e.g., Owen et al. 1990; Sparks et al. 1992). Since the brightest emission on the counterjet side is at the extremity of the radio lobe (like in FRIIs), M87 could be classified as a hybrid radio morphology source. Its radio luminosity ($L_{178} = 1 \times 10^{25} \text{ W m}^{-2}$) also places it close to the FRI/FRII division (Biretta et al. 1999). Kovalev et al. (2007) have observed a very short, weak radio counterjet on parsec-scales in M87, but perhaps that is just a slower outer sheath that quickly terminates.

If indeed some of the extremely misaligned sources are “hybrid” sources, the lack of a correlation between jet misalignment and environment appears to contradict the suggestion that asymmetries in galactic environments, which increase with redshift (e.g., Best et al. 1999), give rise to hybrid morphology sources (e.g., Gopal-Krishna & Wiita 2000; Miller & Brandt 2009). Moreover, the fraction of such sources would be higher in the MOJAVE (6% – 8%), than that reported for the FIRST survey (1%, Gawroński et al. 2006), suggesting that hybrid sources may not be as rare as previously supposed. It is also interesting to note that not many MOJAVE “hybrid” morphology sources fall in the FRI/II luminosity range, but rather have FRII luminosities. In other words, the MOJAVE “hybrid” morphology sources are not necessarily “hybrid” in terms of radio power, but mostly fall into the FRII luminosity class. Chandra X-ray observations of these sources could resolve some of these apparent contradictions.

4.7. Core-only Sources

About 7% of the MOJAVE sources do not show any extended radio emission in our 1.4 GHz VLA A-array images. However the ratio of their 5 GHz radio flux density to their B-band optical flux density is of the order of a few hundred, placing them firmly in the radio-loud AGN class (e.g., Kellermann et al. 1989). The dynamic range achieved in the radio images of these sources varied from about 6000:1 (e.g., 0955+476) to 30,000:1 (e.g., 0202+149), being typically of the order of 10,000:1. While some sources, like 1749+096, failed to reveal any extended emission in a number of different datasets (see also Rector & Stocke 2001), we did detect faint halo-like emission around 1548+056, which was listed as a core-only source by Murphy et al. (1993). Note that observations with the VLA A-array-only are likely to miss very diffuse radio structure, due to the lack of short baselines. We believe therefore that these core-only sources probably have associated faint emission which require more sensitive observations to detect.

The observed fraction of core-only sources in MOJAVE is smaller than that reported for other quasar surveys (20%, Gower & Hutchings 1984; Padrielli et al. 1988). While the core-only sources could have been affected by the redshift surface brightness dimming effect, our discussion in the previous section argues against this conjecture. Alternatively, these sources could just be normal quasars at very small angles to line of sight, so that the VLA resolution is insufficient to delineate the various components. This appears to be the case in 1038+064, and 1417+385, where a two Gaussian component model fits the “core” emission better than a single one. The hypothesis that at least some of these quasars could be beamed FRIs also cannot be ruled out (e.g., Heywood et al. 2007).

4.8. Optical Polarization Subclasses

Low optical polarization radio quasars (LPRQs) consistently reveal core optical fractional polarization, $m_{opt} < 3\%$, while the high optical polarization quasars (HPQs) routinely reveal highly polarized optical cores with $m_{opt} \geq 3\%$ (Angel & Stockman 1980). The classification of the MOJAVE sources into these categories is listed in Table 1, and were obtained from Impey et al. (1991) and Lister & Smith (2000). In all, there are 38 HPQs and 16 LPRQs in the MOJAVE sample. We find no statistically significant differences in the core or extended radio luminosity between LPRQs and HPQs. In Kharb et al. (2008a) we had noted a difference in the integrated (single-dish) 1.4 GHz radio luminosity between LPRQs and HPQs for redshifts less than one. We do not find a difference in the total radio luminosity using the present higher resolution VLA observations. Furthermore, we do not find a statistically significant difference in jet misalignment between LPRQs and HPQs. The

parsec-scale apparent jet speeds of HPQs, however, are systematically higher than those in LPRQs (Kolmogorov-Smirnov test probability that the speeds in HPQs and LPRQs are similar, is $p=0.03$). Additional optical polarimetry information on the sample is needed to further investigate these trends.

5. SUMMARY AND CONCLUSIONS

1. We describe the results from a study of the extended emission at 1.4 GHz in the MOJAVE sample of 135 blazars. New VLA A-array images of six MOJAVE quasars, and previously unpublished VLA A-array archival images of 21 blazars, are presented. The kiloparsec-scale structures are varied, with many sources displaying peculiar, distorted morphologies. Many blazar jets show parsec-to-kiloparsec-scale jet misalignments greater than 90° . These characteristics have been reported in other quasar surveys as well. The 90° bump in the jet misalignment distribution (of which we observe a weak signature) has been suggested to be a result of low-pitch helical parsec-scale jets in the literature.
2. A substantial number of MOJAVE quasars ($\sim 22\%$) and BL Lacs ($\sim 23\%$) display radio powers that are intermediate between FRIs and FRIIs. Many BL Lacs have extended luminosities ($\sim 27\%$) and hot spots ($\sim 60\%$) like quasars. The hypothesis that at least some of the core-only quasars are in fact FRI quasars, cannot be discarded. In terms of radio properties alone, it is difficult to draw a sharp dividing line between BL Lacs and quasars, in the MOJAVE sample. This could be a result of the MOJAVE selection effects which naturally pick sources with a large range in intrinsic radio power (low power quasars and high power BL Lacs), and preferentially bent jets. While the quasars and BL Lacs display a smooth continuation in all their properties, the correlation test results differ sometimes when they are considered separately. This can be understood if the BL Lacs did not constitute a homogeneous population like the quasars, but had both FRI and FRII radio galaxies as their parent population. These findings challenge the simple radio-loud unified scheme, which links FRI sources to BL Lac objects and FRIIs to quasars.
3. We find that there is a significant correlation between extended radio luminosity and apparent parsec-scale jet speeds. This implies that most quasars have faster jets than most BL Lac objects. The large overlap between many properties of quasars and BL Lacs (e.g., 1.4 GHz radio power, parsec-scale jet speeds) however suggests that, at least in terms of radio jet properties, the distinction between these two AGN classes, at an emission-line equivalent width of 5\AA , is essentially an arbitrary one.

4. These observations suggest that the mechanism for the production of optical-UV photons that ionise the emission-line clouds is decoupled from the mechanism that produces powerful radio jets (e.g., Xu et al. 1999; Landt et al. 2006). An alternate hypothesis could be that, BL Lacs with high radio powers are present in dense confining environments, which would increase the radiative losses in them and make them brighter, while the radio quasars with low radio powers are old, field sources. Environmental radio boosting (Barthel & Arnaud 1996) could also explain why the Fanaroff-Riley dividing line is blurred in the MOJAVE sample. X-ray cluster studies could be used to test these ideas.
5. The ratio of the radio core luminosity to the k -corrected optical luminosity (R_v) appears to be a better indicator of jet orientation than the traditionally used radio core prominence parameter (R_c). This seems to be a consequence of the environmental contribution to the extended radio luminosity, used in R_c . Trends with R_v reveal that even though the sample comprises largely of blazars, there is a reasonable range of orientations present in the sample.
6. Trends with the “environment” proxy indicator, L_{ext}/M_{abs} , reveal that jet speeds seem to not depend on the environment on kiloparsec scales, while the jet misalignments seem to be inversely correlated. The jet misalignments are also not correlated with redshift. It appears that the parsec-to-kiloparsec jet misalignment, the parsec-scale jet speeds and to an extent the extended emission (which is related to jet speed) are controlled by factors intrinsic to the AGN. Black hole spins could dictate the jet speeds, while the presence of binary black holes, or kicks imparted to black holes via black hole mergers could influence the jet direction. This is consistent with radio morphologies similar to precessing jet models of Gower et al. (1982) present in the MOJAVE sample, and the signature of the 90° bump in the jet misalignment distribution, which is attributed to low-pitch helical parsec-scale jets.
7. If some of the highly misaligned sources (jet misalignment $\sim 180^\circ$) are “hybrid” FRI+II morphology sources, then the fraction of such sources is higher in the MOJAVE survey (6% – 8%), than that reported for the FIRST survey (1%, Gawroński et al. 2006). Furthermore, the lack of a correlation between jet misalignment and the environmental indicator would appear to contradict the suggestion that hybrid morphology is a result of the jet interacting with an asymmetric environment. X-ray observations of hybrid sources are needed to resolve these issues.
8. About 7% of the MOJAVE quasars show no extended radio emission. We expect more sensitive radio observations to detect faint emission in these sources, as we have detected in the case of 1548+056, previously classified as a core-only quasar. The

hypothesis that at least some of these quasars could be beamed FRIs cannot be ruled out.

9. While the extended radio power or jet misalignments do not show statistically significant differences between the two quasar optical polarization subclasses, *viz.*, LPRQs and HPQs, the parsec-scale apparent jet speeds of HPQs are systematically higher than those in LPRQs.

Table 1. The MOJAVE sample

Source name (1)	z (2)	V mag (3)	Type (4)	Opt Pol (5)	I_{peak} Jy beam $^{-1}$ (6)	I_{rms} Jy beam $^{-1}$ (7)	Freq GHz (8)	β_{app} (9)	S_{core} Jy (10)	S_{ext} mJy (11)	Radio Morph (12)	PcjetPA Degree (13)	KpcjetPA Degree (14)	Ref (15)
0003-066	0.347	18.50	B	Y	2.605	1.6×10^{-4}	1.4000	2.89	2.66	43.9	2	282	15	AL634*
0007+106	0.0893	15.40	G	...	0.075	4.0×10^{-5}	1.4000	0.97	0.08	17.6	2hs	284	239	AL634*
0016+731	1.781	19.00	Q	N	0.398	4.2×10^{-4}	1.4000	6.74	0.40	7.8	1hs	132	2	AL634*
0048-097	17.44	B	Y	0.562	1.8×10^{-4}	1.4250	0.57	139.7	1hs+2, 2hs	337	190	AB1141
0059+581	0.644	17.30	Q	...	1.554	1.1×10^{-4}	1.4000	11.08	1.57	19.4	ch+1	236	AL634*
0106+013	2.099	18.39	Q	Y	2.760	1.4×10^{-4}	1.4000	26.50	2.81	530.6	1hs, 2	238	184	AL634*
0109+224	0.265	15.66	B	Y	0.361	7.8×10^{-5}	1.4000	0.36	3.9	1	82	93	AL634*
0119+115	0.57	19.70	Q	...	1.188	9.8×10^{-5}	1.4000	17.09	1.24	113.7	1hs, ch	6	33	AL634*
0133+476	0.859	19.50	Q	Y	1.872	9.6×10^{-5}	1.4000	12.98	1.88	8.7	1hs	331	340	AL634*
0202+149 ^c	0.405	21.00	Q	Y	3.808	1.4×10^{-4}	1.4000	6.41	3.86	1.1	c	319	AL634*
0202+319	1.466	17.40	Q	N	0.648	8.4×10^{-5}	1.4000	8.30	0.65	11.7	1hs	357	2	AL634*
0212+735	2.367	19.00	Q	Y	2.458	1.0×10^{-4}	1.4000	7.63	2.47	1.7	1hs, 2hs	122	253	AL634*
0215+015	1.715	16.09	B	Y	0.416	6.9×10^{-5}	1.4000	34.16	0.45	71.1	2hs	104	92	AL634*
0224+671	0.523	19.50	Q	...	1.476	1.0×10^{-4}	1.4000	11.63	1.48	149.2	2hs	355	184	AL634*
0234+285	1.213	19.30	Q	Y	2.274	1.0×10^{-4}	1.4000	12.31	2.33	99.9	1hs	349	331	AL634*
0235+164	0.94	15.50	B	Y	1.501	5.8×10^{-5}	1.4000	1.51	25.5	1hs+2	325	343	AL634*
0238-084	0.005	12.31	G	...	1.091	6.0×10^{-5}	1.4000	0.34	1.11	111.3	2	66	275	AL634*
0300+470	16.95	B	Y	1.166	5.7×10^{-5}	1.4000	1.18	60.1	1, ch	148	225	AL634*
0316+413	0.0176	12.48	G	N	20.76	1.0×10^{-3}	1.3121	0.31	21.40	1103.0	2hs	178	158	BT024
0333+321	1.263	17.50	Q	N	2.994	1.0×10^{-4}	1.4000	12.78	3.02	71.8	1hs	126	149	AL634*
0336-019	0.852	18.41	Q	Y	2.908	1.5×10^{-4}	1.4000	22.36	2.92	70.3	1hs	67	344	AL634*
0403-132	0.571	17.09	Q	Y	4.043	3.3×10^{-4}	1.4000	19.69	4.33	9.1	1hs+2	155	202	AL634*
0415+379	0.0491	18.05	G	...	0.542	5.7×10^{-4}	1.4899	5.86	0.57	2700.0	2hs	71	62	AR102
0420-014	0.914	17.00	Q	Y	2.887	1.0×10^{-4}	1.4000	7.34	2.91	70.2	2hs, 1hs+2	183	189	AL634*
0422+004	16.98	B	Y	1.083	1.3×10^{-4}	1.4000	1.09	6.1	2hs	357	200	AL634*
0430+052	0.033	15.05	G	...	2.845	1.7×10^{-4}	1.4649	5.38	2.95	159.5	1, 2	252	293	AB379
0446+112	20.00	U	...	1.527	1.2×10^{-4}	1.4000	1.56	15.4	1hs	103	207	AL634*
0458-020	2.286	18.06	Q	Y	1.629	3.8×10^{-4}	1.4899	16.51	1.66	148.1	1hs, 2hs	321	230	AN047
0528+134	2.06	20.00	Q	...	2.204	1.2×10^{-4}	1.4000	19.14	2.24	60.1	2hs, 1hs+2	19	261	AL634*
0529+075	1.254	19.00	Q	...	1.518	5.7×10^{-5}	1.4000	12.66	1.54	126.8	2hs, 1hs+2	353	221	AL634*
0529+483	1.162	19.90	Q	...	0.641	6.7×10^{-5}	1.4000	19.78	0.65	21.5	1hs+2	32	75	AL634*
0552+398 ^c	2.363	18.30	Q	...	1.539	1.0×10^{-4}	1.4000	0.36	1.55	1.2	c	290	AL634*
0605-085	0.872	17.60	Q	...	2.344	2.8×10^{-4}	1.4250	19.79	1.20	123.9	1hs	109	99	AD298
0607-157 ^c	0.324	18.00	Q	...	3.011	1.4×10^{-4}	1.4000	3.94	3.02	1.1	c	52	AL634*
0642+449 ^c	3.396	18.49	Q	...	0.644	7.5×10^{-5}	1.4000	0.75	0.65	1.4	c	90	AL634*
0648-165	U	...	2.085	1.4×10^{-4}	1.4000	2.12	11.2	c, 1	273	272	AL634*
0716+714	0.31	15.50	B	Y	0.645	6.8×10^{-5}	1.4000	10.06	0.69	376.4	2hs, 1hs+2	40	300	AQ006
0727-115	1.591	20.30	Q	...	3.182	9.4×10^{-5}	1.4250	3.22	2.4	c, 1hs	292	AC874†
0730+504	0.72	19.30	Q	...	0.676	6.0×10^{-5}	1.4250	14.06	0.69	82.5	2hs	210	82	AC874†
0735+178	16.22	B	Y	1.92	0.7×10^{-3}	1.4650	1.91	20.6	1	77	165	Murphy
0736+017	0.191	16.47	Q	Y	2.327	3.2×10^{-4}	1.4899	14.44	2.34	40.9	2hs	273	297	AA025
0738+313	0.631	16.92	Q	...	2.16	0.4×10^{-3}	1.4650	10.75	2.16	65.0	2hs	156	166	Murphy
0742+103	2.624	24.00	Q	...	3.600	2.3×10^{-4}	1.4899	3.62	5.8	1, 2	354	81	AY012
0748+126	0.889	18.70	Q	...	1.43	0.5×10^{-3}	1.4650	18.36	1.43	27.0	2hs	110	125	Murphy
0754+100	0.266	15.00	B	Y	2.07	0.4×10^{-3}	1.4650	14.40	2.07	6.7	2hs	10	293	Murphy
0804+499	1.436	19.20	Q	Y	0.64	0.3×10^{-3}	1.4650	1.82	0.64	5.3	1hs	134	Murphy
0805-077	1.837	19.80	Q	...	1.439	5.8×10^{-5}	1.4250	50.60	1.58	59.8	1hs	332	278	AC874†
0808+019	1.148	17.20	B	Y	0.449	9.1×10^{-5}	1.4899	12.99	0.46	18.2	2hs	182	200	AA025
0814+425	0.245	18.18	B	Y	1.015	3.1×10^{-4}	1.5159	1.70	1.03	76.8	2hs	136	322	AK460
0823+033	0.506	16.80	B	Y	1.33	0.4×10^{-3}	1.4650	17.80	1.32	4.1	1hs	15	Murphy
0827+243	0.94	17.26	Q	...	0.743	1.4×10^{-4}	1.5100	21.97	0.76	62.7	1hs+2	135	199	AV150
0829+046	0.174	16.40	B	Y	0.788	1.9×10^{-4}	1.4000	10.10	0.80	150.8	2, 1hs+2	60	151	AG618
0836+710	2.218	17.30	Q	N	3.168	1.7×10^{-4}	1.4000	25.38	3.34	73.6	1	211	205	AL634*
0838+133	0.681	18.15	Q	...	0.287	8.0×10^{-5}	1.4250	12.93	0.35	2216.6	2hs	76	94	AH480
0851+202	0.306	15.43	B	Y	1.563	1.4×10^{-4}	1.5315	15.17	1.57	10.7	1hs, 1	260	251	AS764
0906+015	1.024	17.31	Q	Y	1.00	0.4×10^{-3}	1.4650	20.66	1.00	38.0	1hs	46	54	Murphy
0917+624	1.446	19.50	Q	...	1.11	0.4×10^{-3}	1.4650	15.57	1.11	6.4	1hs+2	341	234	Murphy
0923+392	0.695	17.03	Q	N	2.399	3.1×10^{-4}	1.5524	4.29	2.83	361.8	1hs+2	98	83	AB310
0945+408	1.249	18.05	Q	N	1.23	0.9×10^{-3}	1.4650	18.60	1.23	95.0	1hs	114	32	Murphy
0955+476 ^c	1.882	18.65	Q	...	0.606	1.0×10^{-4}	1.4899	2.48	0.62	1.1	c	124	270	AP188
1036+054	0.473	Q	...	0.916	4.9×10^{-5}	1.4250	6.14	0.94	57.0	1hs+2	350	226	AC874†
1038+064	1.265	16.70	Q	...	1.465	1.5×10^{-4}	1.6649	11.86	1.49	11.0	1	146	166	GX007
1045-188	0.595	18.20	Q	...	0.726	6.6×10^{-5}	1.4250	8.57	0.76	509.4	1hs+2	146	125	AC874†
1055+018	0.89	18.28	Q	Y	2.675	1.5×10^{-4}	1.4250	10.99	2.70	230.8	2hs	300	186	AB631
1124-186	1.048	18.65	Q	...	0.652	1.9×10^{-4}	1.4250	0.66	12.3	1hs	170	134	AD337

Table 1—Continued

Source name (1)	z (2)	V mag (3)	Type (4)	Opt Pol (5)	I_{peak} Jy beam $^{-1}$ (6)	I_{rms} Jy beam $^{-1}$ (7)	Freq GHz (8)	β_{app} (9)	S_{core} Jy (10)	S_{ext} mJy (11)	Radio Morph (12)	PcjetPA Degree (13)	KpcjetPA Degree (14)	Ref (15)
1127–145	1.184	16.90	Q	...	4.460	2.3×10^{-4}	1.4649	14.17	4.58	59.3	1hs	66	44	AB37
1150+812	1.25	19.40	Q	...	1.874	6.5×10^{-4}	1.4000	7.08	1.89	89.2	1hs+2, 2	163	257	AL63
1156+295	0.729	14.41	Q	Y	1.433	2.4×10^{-4}	1.4899	24.85	1.55	196.1	2, 1hs+2	14	344	AA02
1213–172	21.40	U	...	1.676	1.0×10^{-4}	1.4250	1.85	119.3	1	117	266	AC87
1219+044	0.965	17.98	Q	...	0.548	5.9×10^{-5}	1.4250	2.34	0.60	155.5	1hs+2	172	0	AC87
1222+216	0.432	17.50	Q	...	0.930	8.0×10^{-5}	1.4000	21.02	1.10	956.4	2hs	351	76	AL63
1226+023	0.158	12.85	Q	N	34.26	1.5×10^{-3}	1.3659	13.44	34.89	17671	1hs	238	222	AE10
1228+126	0.0044	12.86	G	...	3.558	2.3×10^{-4}	1.6649	0.032	3.88	115012	2	291	67	BC07
1253–055	0.536	17.75	Q	Y	10.17	6.4×10^{-4}	1.6649	20.58	10.56	2095.0	2hs	245	201	W088
1308+326	0.996	15.24	Q	Y	1.321	1.5×10^{-4}	1.4000	27.14	1.33	69.1	2hs, 1hs+2	284	359	AL63
1324+224	1.4	18.90	Q	...	1.128	9.6×10^{-5}	1.4000	1.14	20.4	1hs	343	237	AL63
1334–127	0.539	19.00	Q	Y	1.992	9.9×10^{-5}	1.4899	10.26	2.07	151.0	1hs, 1hs+2	147	106	AD17
1413+135	0.247	20.50	B	...	1.056	1.1×10^{-4}	1.4899	1.79	1.08	5.8	2	55	256	AC30
1417+385	1.831	19.69	Q	...	0.506	6.4×10^{-5}	1.4000	15.44	0.52	2.5	1	164	123	AL63
1458+718	0.905	16.78	Q	N	5.760	8.7×10^{-4}	1.4000	7.05	7.57	68.9	c, 1	164	11	AL63
1502+106	1.839	18.56	Q	Y	1.795	7.9×10^{-5}	1.4000	14.77	1.82	38.3	1hs	116	159	AL63
1504–166	0.876	18.50	Q	Y	2.354	4.0×10^{-4}	1.4899	4.31	2.39	11.4	1hs, 2hs	165	164	AY01
1510–089	0.36	16.54	Q	Y	1.380	1.0×10^{-4}	1.4899	20.15	1.45	180.2	1hs, 2hs	328	163	AY01
1538+149	0.605	17.30	B	Y	1.479	6.0×10^{-5}	1.4000	8.73	1.67	71.4	ch, 1	323	320	AL63
1546+027	0.414	17.45	Q	Y	1.15	0.4×10^{-3}	1.4650	12.07	1.15	18.8	1hs+2	170	162	Murp
1548+056	1.422	19.50	Q	Y	2.106	1.6×10^{-4}	1.5524	11.56	2.21	42.9	ch	8	AB31
1606+106	1.226	18.70	Q	...	1.35	1.3×10^{-3}	1.4650	18.90	1.35	26.5	1hs	332	271	Murp
1611+343	1.397	18.11	Q	N	2.83	0.5×10^{-3}	1.4650	14.09	2.83	20.6	2hs	166	194	Murp
1633+382	1.814	18.00	Q	Y	2.17	0.4×10^{-3}	1.4650	29.46	2.17	32.0	1hs+2	284	176	Murp
1637+574	0.751	16.90	Q	N	0.996	1.1×10^{-4}	1.5524	10.61	1.01	71.2	1hs	198	282	AB31
1638+398	1.666	19.37	Q	...	1.147	2.0×10^{-4}	1.4899	12.27	1.17	27.6	2hs	300	150	AR25
1641+399	0.593	16.62	Q	Y	7.153	1.3×10^{-3}	1.5149	19.27	7.95	1476.9	1hs+2, 2hs	288	327	AS390
1655+077	0.621	20.00	Q	Y	1.199	1.4×10^{-4}	1.5524	14.44	1.27	199.1	1hs+2	314	269	AB31
1726+445	0.717	18.10	Q	...	0.993	1.3×10^{-4}	1.4899	1.81	1.00	55.3	1hs+2	271	328	AK13
1730–130	0.902	19.50	Q	...	6.101	3.4×10^{-4}	1.4250	35.69	6.13	517.8	2hs, 1hs+2	2	273	AL26
1739+522	1.375	18.70	Q	Y	1.571	1.5×10^{-4}	1.4899	1.61	27.6	1hs+2	15	262	AC30
1741–038 ^c	1.054	20.40	Q	Y	1.677	1.5×10^{-4}	1.4250	1.70	3.5	c	201	134	AL26
1749+096 ^c	0.322	16.78	B	Y	1.039	1.6×10^{-4}	1.4899	6.84	1.05	4.9	c	38	AC30
1751+288	1.118	19.60	Q	...	0.265	1.7×10^{-4}	1.4350	3.07	0.27	8.1	2, 1	349	40	AS65
1758+388	2.092	17.98	Q	...	0.327	1.7×10^{-4}	1.5149	2.38	0.33	3.2	1hs+2	266	270	AS390
1800+440	0.663	17.90	Q	...	0.465	2.1×10^{-4}	1.5149	15.41	0.50	246.6	1hs+2	203	239	AS390
1803+784	0.68	15.90	B	Y	1.969	1.0×10^{-4}	1.4000	8.97	1.98	20.8	2hs	266	192	AL63
1807+698	0.051	14.22	B	Y	1.133	1.1×10^{-4}	1.5149	0.10	1.20	368.7	1hs	261	242	AB70
1823+568	0.664	19.30	B	Y	0.873	6.1×10^{-4}	1.4250	20.85	0.95	137.4	2	201	94	AM67
1828+487	0.692	16.81	Q	N	5.140	6.3×10^{-4}	1.5524	13.65	8.21	5431.2	2hs	310	119	AB31
1849+670	0.657	16.90	Q	...	0.468	1.1×10^{-4}	1.4000	30.63	0.47	101.0	1hs+2	308	209	AL63
1928+738	0.302	16.06	Q	N	3.186	1.6×10^{-4}	1.4000	8.43	3.22	356.5	1hs+2, 2hs	164	165	AL63
1936–155	1.657	20.30	Q	Y	1.064	1.8×10^{-4}	1.4899	2.59	1.08	10.5	1hs+2, 2	180	214	AD16
1957+405	0.0561	15.10	G	...	33.56 [‡]	6.5×10^{-3}	1.5245	0.21	0.65	1.4×10^6	2hs	282	291	AC16
1958–179 ^c	0.65	18.60	Q	Y	1.789	1.5×10^{-4}	1.4899	1.89	1.82	9.4	c	207	AA07
2005+403	1.736	19.00	Q	...	2.420	5.1×10^{-4}	1.6657	12.21	2.47	10.6	1hs+2	127	137	AK40
2008–159	1.18	18.30	Q	...	0.546	1.0×10^{-4}	1.4899	7.98	0.55	7.5	1hs	7	5	AK24
2021+317	U	...	2.968	6.8×10^{-4}	1.6657	3.06	132.9	ch, 1	201	AK40
2021+614	0.227	19.00	G	N	2.647	2.9×10^{-4}	1.4899	0.41	2.67	1.3	2	33	AM17
2037+511	1.686	21.00	Q	...	4.604	6.4×10^{-4}	1.6657	3.29	4.97	657.6	1hs	214	327	AK40
2121+053	1.941	20.40	Q	Y	1.08	0.6×10^{-3}	1.4650	13.28	1.08	4.8	1, 1hs	271	Murp
2128–123	0.501	16.11	Q	N	1.393	1.3×10^{-4}	1.4899	6.94	1.42	39.8	1hs+2	209	190	AY01
2131–021	1.285	19.00	B	Y	1.320	1.3×10^{-4}	1.5149	20.03	1.37	151.9	2hs	108	137	AB70
2134+004	1.932	17.11	Q	N	4.82	0.4×10^{-3}	1.4650	5.93	4.82	6.6	1hs	266	298	Murp
2136+141 ^c	2.427	18.90	Q	...	1.131	1.4×10^{-4}	1.5524	5.43	1.14	0.8	c	205	AB31
2145+067	0.99	16.47	Q	N	2.840	1.7×10^{-4}	1.4000	2.49	2.87	27.7	1hs, 1	119	313	AL63
2155–152	0.672	18.30	Q	Y	2.627	1.5×10^{-4}	1.4000	18.11	2.70	304.7	1hs+2	214	195	AL63
2200+420	0.0686	14.72	B	Y	1.970	7.0×10^{-5}	1.4000	10.57	1.99	14.2	2, 1hs+2	182	143	AL63
2201+171	1.075	19.50	Q	...	0.820	5.8×10^{-5}	1.4000	2.54	0.87	74.6	1hs, 2hs	45	267	AL63
2201+315	0.295	15.58	Q	N	1.517	1.3×10^{-4}	1.4000	7.87	1.54	378.4	2hs	219	251	AL63
2209+236 ^c	1.125	20.66	Q	...	0.425	4.9×10^{-5}	1.4000	3.43	0.43	0.9	c	54	AL63
2216–038	0.901	16.38	Q	...	1.722	1.1×10^{-4}	1.4000	5.62	1.76	312.7	2hs	190	143	AL63
2223–052	1.404	18.39	Q	Y	6.769	3.4×10^{-4}	1.4000	17.33	7.13	91.6	1	99	335	AL63
2227–088	1.56	17.43	Q	Y	0.920	4.2×10^{-5}	1.4000	8.14	0.93	8.4	1hs	348	314	AL63
2230+114	1.037	17.33	Q	Y	6.633	3.7×10^{-4}	1.4000	15.41	6.99	148.0	1	147	144	AL63

We would like to thank the anonymous referee for a careful assessment of the manuscript, which has led to significant improvement. PK would like to thank John Peterson for useful discussions on galaxy clusters, and Chris O’Dea for insightful suggestions. The MOJAVE project is supported under National Science Foundation grant 0807860-AST and NASA-Fermi grant NNX08AV67G. This research has made use of the NASA/IPAC Extragalactic Database (NED) which is operated by the Jet Propulsion Laboratory, California Institute of Technology, under contract with the National Aeronautics and Space Administration. The National Radio Astronomy Observatory is a facility of the National Science Foundation operated under cooperative agreement by Associated Universities, Inc.

REFERENCES

Abdo, A. A. et al., 2009, ApJ, 700, 597

Alberdi, A., Marcaide, J. M., Marscher, A. P., Zhang, Y. F., Elosegui, P., Gomez, J. L., & Shaffer, D. B. 1993, ApJ, 402, 160

Angel, J. R. P., & Stockman, H. S. 1980, ARA&A, 18, 321

Antonucci, R. R. J., & Ulvestad, J. S. 1985, ApJ, 294, 158

Appl, S., Sol, H., & Vicente, L. 1996, A&A, 310, 419

Barthel, P. D., & Arnaud, K. A. 1996, MNRAS, 283, L45

Barthel, P. D., & Miley, G. K. 1988, Nature, 333, 319

Baum, S. A., Zirbel, E. L., & O’Dea, C. P. 1995, ApJ, 451, 88

Begelman, M. C., Blandford, R. D., & Rees, M. J. 1980, Nature, 287, 307

Best, P. N., Eales, S. A., Longair, M. S., Rawlings, S., & Rottgering, H. J. A. 1999, MNRAS, 303, 616

Bicknell, G. V. 1995, ApJS, 101, 29

Biretta, J. A., Sparks, W. B., & Macchetto, F. 1999, ApJ, 520, 621

Bîrzan, L., Rafferty, D. A., McNamara, B. R., Wise, M. W., & Nulsen, P. E. J. 2004, ApJ, 607, 800

Blandford, R. D., & Konigl, A. 1979, ApJ, 232, 34

Blanton, E. L., Gregg, M. D., Helfand, D. J., Becker, R. H., & White, R. L. 2000, ApJ, 531, 118

Böhringer, H., Schuecker, P., Guzzo, L., Collins, C. A., Voges, W., Cruddace, R. G., Ortiz-Gil, A., Chincarini, G., De Grandi, S., Edge, A. C., MacGillivray, H. T., Neumann, D. M., Schindler, S., & Shaver, P. 2004, A&A, 425, 367

Brotherton, M. S. 1996, ApJS, 102, 1

Cara, M., & Lister, M. L. 2008, ApJ, 674, 111

Cohen, M. H., Lister, M. L., Homan, D. C., Kadler, M., Kellermann, K. I., Kovalev, Y. Y., & Vermeulen, R. C. 2007, ApJ, 658, 232

Conway, J. E., & Murphy, D. W. 1993, ApJ, 411, 89

Cooper, N. J., Lister, M. L., & Kochanczyk, M. D. 2007, ApJS, 171, 376

Corbett, E. A., Robinson, A., Axon, D. J., Hough, J. H., Jeffries, R. D., Thurston, M. R., & Young, S. 1996, MNRAS, 281, 737

Ebeling, H., Edge, A. C., Bohringer, H., Allen, S. W., Crawford, C. S., Fabian, A. C., Voges, W., & Huchra, J. P. 1998, MNRAS, 301, 881

Fanaroff, B. L., & Riley, J. M. 1974, MNRAS, 167, 31P

Gawroński, M. P., Marecki, A., Kunert-Bajraszewska, M., & Kus, A. J. 2006, A&A, 447, 63

Ghisellini, G., & Celotti, A. 2001, A&A, 379, L1

Ghisellini, G., Tavecchio, F., & Ghirlanda, G. 2009, MNRAS, 1261, ArXiv e-prints 0906.2195

Giroletti, M., Giovannini, G., Taylor, G. B., & Falomo, R. 2004, ApJ, 613, 752

Gopal-Krishna, & Wiita, P. J. 2000, A&A, 363, 507

Gower, A. C., Gregory, P. C., Unruh, W. G., & Hutchings, J. B. 1982, ApJ, 262, 478

Gower, A. C., & Hutchings, J. B. 1984, AJ, 89, 1658

Hardcastle, M. J., & Sakelliou, I. 2004, MNRAS, 349, 560

Harris, D. E., Dewdney, P. E., Costain, C. H., Butcher, H., & Willis, A. G. 1983, ApJ, 270,

Heywood, I., Blundell, K. M., & Rawlings, S. 2007, MNRAS, 381, 1093

Hintzen, P., Ulvestad, J., & Owen, F. 1983, AJ, 88, 709

Homan, D. C., Ojha, R., Wardle, J. F. C., Roberts, D. H., Aller, M. F., Aller, H. D., & Hughes, P. A. 2002, ApJ, 568, 99

Impey, C. D., Lawrence, C. R., & Tapia, S. 1991, ApJ, 375, 46

Jetha, N. N., Hardcastle, M. J., & Sakelliou, I. 2006, MNRAS, 368, 609

Kapahi, V. K., & Saikia, D. J. 1982, Journal of Astrophysics and Astronomy, 3, 465

Kellermann, K. I., Lister, M. L., Homan, D. C., Vermeulen, R. C., Cohen, M. H., Ros, E., Kadler, M., Zensus, J. A., & Kovalev, Y. Y. 2004, ApJ, 609, 539

Kellermann, K. I., Sramek, R., Schmidt, M., Shaffer, D. B., & Green, R. 1989, AJ, 98, 1195

Kharb, P., Lister, M. L., & Shastri, P. 2008a, International Journal of Modern Physics D, 17, 1545

Kharb, P., O'Dea, C. P., Baum, S. A., Daly, R. A., Mory, M. P., Donahue, M., & Guerra, E. J. 2008b, ApJS, 174, 74

Kharb, P., & Shastri, P. 2004, A&A, 425, 825

Kollgaard, R. I., Wardle, J. F. C., Roberts, D. H., & Gabuzda, D. C. 1992, AJ, 104, 1687

Kovalev, Y. Y., Lister, M. L., Homan, D. C., & Kellermann, K. I. 2007, ApJ, 668, L27

Landt, H., & Bignall, H. E. 2008, MNRAS, 391, 967

Landt, H., Padovani, P., Perlman, E. S., & Giommi, P. 2004, MNRAS, 351, 83

Landt, H., Perlman, E. S., & Padovani, P. 2006, ApJ, 637, 183

Laurent-Muehleisen, S. A., Kollgaard, R. I., Feigelson, E. D., Brinkmann, W., & Siebert, J. 1999, ApJ, 525, 127

Ledlow, M. J., & Owen, F. N. 1996, AJ, 112, 9

Lister, M. L., Aller, H. D., Aller, M. F., Cohen, M. H., Homan, D. C., Kadler, M., Kellermann, K. I., Kovalev, Y. Y., Ros, E., Savolainen, T., Zensus, J. A., & Vermeulen, R. C. 2009a, AJ, 137, 3718

Lister, M. L., Homan, D. C., Kadler, M., Kellermann, K. I., Kovalev, Y. Y., Ros, E., Savolainen, T., & Zensus, J. A. 2009b, ApJ, 696, L22

Lister, M. L., & Smith, P. S. 2000, ApJ, 541, 66

Maraschi, L., Foschini, L., Ghisellini, G., Tavecchio, F., & Sambruna, R. M. 2008, MNRAS, 391, 1981

McCarthy, P. J. 1993, ARA&A, 31, 639

Meier, D. L. 1999, ApJ, 522, 753

Merritt, D., & Ekers, R. D. 2002, Science, 297, 1310

Miller, B. P., & Brandt, W. N. 2009, ApJ, 695, 755

Miller, J. S., French, H. B., & Hawley, S. A. 1978, in BL Lac Objects, ed. A. M. Wolfe, 176–187

Murphy, D. W., Browne, I. W. A., & Perley, R. A. 1993, MNRAS, 264, 298

Napier, P. J., Thompson, A. R., & Ekers, R. D. 1983, IEEE Proceedings, 71, 1295

Nieppola, E., Tornikoski, M., & Valtaoja, E. 2006, A&A, 445, 441

O'Dea, C. P., Baum, S. A., & Stanghellini, C. 1991, ApJ, 380, 66

O'Donoghue, A. A., Owen, F. N., & Eilek, J. A. 1990, ApJS, 72, 75

Orr, M. J. L., & Browne, I. W. A. 1982, MNRAS, 200, 1067

Owen, F. N., Eilek, J. A., & Keel, W. C. 1990, ApJ, 362, 449

Owen, F. N., Ledlow, M. J., & Keel, W. C. 1996, AJ, 111, 53

Padovani, P., & Giommi, P. 1995, ApJ, 444, 567

Padovani, P., & Urry, C. M. 1992, ApJ, 387, 449

Padielli, L., de Ruiter, H. R., & Rogora, A. 1988, A&A, 196, 49

Pearson, T. J., & Readhead, A. C. S. 1988, ApJ, 328, 114

Prestage, R. M., & Peacock, J. A. 1988, MNRAS, 230, 131

Pringle, J. E. 1997, MNRAS, 292, 136

Rawlings, S., & Saunders, R. 1991, *Nature*, 349, 138

Rector, T. A., & Stocke, J. T. 2001, *AJ*, 122, 565

Reynolds, C. S., Fabian, A. C., Celotti, A., & Rees, M. J. 1996, *MNRAS*, 283, 873

Scarpa, R., & Falomo, R. 1997, *A&A*, 325, 109

Schwab, F. R. 1980, *SPIE*, 231, 18

Sparks, W. B., Fraix-Burnet, D., Macchetto, F., & Owen, F. N. 1992, *Nature*, 355, 804

Stickel, M., Fried, J. W., Kuehr, H., Padovani, P., & Urry, C. M. 1991, *ApJ*, 374, 431

Stocke, J. T., Morris, S. L., Gioia, I. M., Maccacaro, T., Schild, R., Wolter, A., Fleming, T. A., & Henry, J. P. 1991, *ApJS*, 76, 813

Urry, C. M., & Padovani, P. 1995, *PASP*, 107, 803

Urry, M. 1999, in *Astronomical Society of the Pacific Conference Series*, Vol. 159, BL Lac Phenomenon, ed. L. O. Takalo & A. Sillanpää, 3

Vermeulen, R. C., Ogle, P. M., Tran, H. D., Browne, I. W. A., Cohen, M. H., Readhead, A. C. S., Taylor, G. B., & Goodrich, R. W. 1995, *ApJ*, 452, L5

Véron-Cetty, M.-P., & Véron, P. 2006, *A&A*, 455, 773

Wills, B. J., & Brotherton, M. S. 1995, *ApJ*, 448, L81

Xu, C., Livio, M., & Baum, S. 1999, *AJ*, 118, 1169

Xu, W., Readhead, A. C. S., Pearson, T. J., Wilkinson, P. N., & Polatidis, A. G. 1994, in Compact Extragalactic Radio Sources, ed. J. A. Zensus & K. I. Kellermann, 7

Yee, H. K. C., & Oke, J. B. 1978, *ApJ*, 226, 753

A. PREVIOUSLY UNPUBLISHED RADIO IMAGES FROM THE ARCHIVE

Table 1—Continued

Source name (1)	z (2)	V mag (3)	Type (4)	Opt Pol (5)	I_{peak} Jy beam $^{-1}$ (6)	I_{rms} Jy beam $^{-1}$ (7)	Freq GHz (8)	β_{app} (9)	S_{core} Jy (10)	S_{ext} mJy (11)	Radio Morph (12)	PcjetPA Degree (13)	KpcjetPA Degree (14)	Ref (15)
2243–123	0.632	16.45	Q	Y	2.247	8.4×10^{-5}	1.4000	5.49	2.27	27.7	1hs	29	44	AL634*
2251+158	0.859	16.10	Q	Y	13.88	4.9×10^{-4}	1.4000	14.19	14.09	822.0	1hs	297	311	AL634*
2331+073	0.401	16.04	Q	...	0.602	4.3×10^{-5}	1.4000	4.47	0.61	38.4	1hs+2	225	251	AL634*
2345–167	0.576	18.41	Q	Y	1.921	8.1×10^{-5}	1.4000	13.45	1.99	142.7	1hs	141	227	AL634*
2351+456	1.986	20.60	Q	...	2.260	6.3×10^{-5}	1.4000	27.09	2.35	6.9	c, 1hs	278	260	AL634*

Note. — Col. 1 & 2: IAU B1950 names of the MOJAVE sources and their redshifts. c = sources do not show any discernable extended emission. Col. 3: Apparent V-band magnitude obtained from the AGN catalog of Véron-Cetty & Véron (2006) or NED. Col. 4: Blazar classification – Q = quasar, B = BL Lac object, G = radio galaxy, U = Unidentified. Col. 5: Highly optically polarized – Y = Yes, N = No, = no data available. Col. 6 & 7: Peak and rms intensity in radio map, respectively. I_{rms} for the sources in Murphy et al. (1993) are the CLEV values in their Table 2. ‡ for Cygnus A, the peak intensity corresponds to the south-eastern hot spot. Col. 8: Central observing frequency in GHz. Col. 9: Apparent parsec-scale speed of the fastest jet feature. Col. 10: Integrated core flux density at ~ 1.4 GHz obtained with JMFIT. Col. 11: Extended flux density obtained by subtracting the core from the total radio flux density. Col. 12: Radio morphology – c = core only, ch = core-halo, 1hs = 1 hot spot, 2hs = 2 hot spots, 1 = 1 sided, 2 = 2 sided, 1hs+2 = 2 sided structure with hot spot on one side. Alternate morphologies are listed separated by commas. Col. 13: Parsec-scale jet position angle. Col. 14: Kiloparsec-scale jet position angle. Col. 15: References and VLA archive Project IDs for the radio data – †=New data presented in this paper. *=Data presented in Cooper et al. (2007). Murphy = Murphy et al. (1993).

Table 2. Correlation Results

Param 1	Param 2	Class	Spearman Coeff	Spearman Prob	Kendall τ Coeff	Kendall τ Prob	Correl ?
(1)	(2)	(3)	(4)	(5)	(6)	(7)	(8)
L_{core}	L_{ext}	ALL	0.61	1.6×10^{-13}	0.45	$< 1 \times 10^{-5}$	YES
M_{abs}	L_{ext}	ALL	-0.39	9.8×10^{-6}	-0.27	1.1×10^{-6}	YES
L_{ext}	β_{app}	ALL	0.44	5.2×10^{-7}	0.31	5.3×10^{-7}	YES
		Q	0.36	0.0004	0.24	0.0005	YES
		B	0.32	0.193	0.24	0.148	NO
M_{abs}	β_{app}	ALL	-0.27	0.0025	-0.18	0.0031	YES
R_c	L_{core}	ALL	0.26	0.003	0.19	0.002	YES
		Q	0.39	8.5×10^{-5}	0.27	8.8×10^{-5}	YES
		B	-0.02	0.912	-0.01	0.909	NO
R_c	L_{ext}	ALL	-0.49	1.5×10^{-8}	-0.35	$< 1 \times 10^{-5}$	YES
R_c	β_{app}	ALL	-0.18	0.046	-0.12	0.044	YES?
		Q	-0.28	0.006	-0.19	0.006	YES
		B	0.02	0.922	0.01	0.939	NO
R_c	ΔPA	ALL	-0.13	0.146	-0.09	0.142	NO
		Q	-0.18	0.087	-0.12	0.082	YES?
		B	-0.15	0.579	-0.10	0.589	NO
R_v	L_{core}	ALL	0.62	6.5×10^{-15}	0.45	$< 1 \times 10^{-5}$	YES
R_v	β_{app}	ALL	0.11	0.200	0.07	0.226	NO
R_v	ΔPA	ALL	0.23	0.011	0.15	0.017	YES?
		Q	0.26	0.011	0.17	0.015	YES?
		B	0.38	0.143	0.23	0.207	NO
		FRII	0.24	0.029	0.16	0.032	YES?
		FRI/II	0.18	0.277	0.11	0.313	NO
		FRI	0.12	0.658	0.07	0.701	NO
ΔPA	z	ALL	0.06	0.514	0.04	0.498	NO
L_{ext}/M_{abs}	z	Q+B	0.21	0.023	0.14	0.021	YES?
		Q	0.27	0.007	0.19	0.007	YES
		B	0.31	0.209	0.16	0.343	NO
L_{ext}/M_{abs}	β_{app}	Q+B	-0.02	0.810	-0.01	0.768	NO
L_{ext}/M_{abs}	ΔPA	Q+B	-0.34	0.0003	-0.23	0.0005	YES

Note. — Cols. 1 & 2: Parameters being examined for correlations. Results from a partial regression analysis are cited in the main text. The ten core-only sources have been excluded from correlations with extended luminosity. Including the upper limits in extended luminosity as detections, does not alter any of the observed trends. Col. 3: The correlation test results have been presented separately if they were different for quasars and BL Lacs considered alone. ALL = quasars + BL Lacs + radio galaxies, Q = only quasars, B = only BL Lacs, Q+B = quasars + BL Lacs. FRII, FRI/II, and FRI are as defined in §4.5. Cols. 4 & 5: Spearman rank correlation coefficient and chance probability. Cols. 6 & 7: Kendall Tau correlation coefficient and chance probability. Col. 8: Indicates if the parameters are significantly correlated. ‘YES?’ indicates a marginal correlation. We note that at the 95% confidence level, 1.7 spurious correlations could arise from the ≈ 35 correlations that we tested.

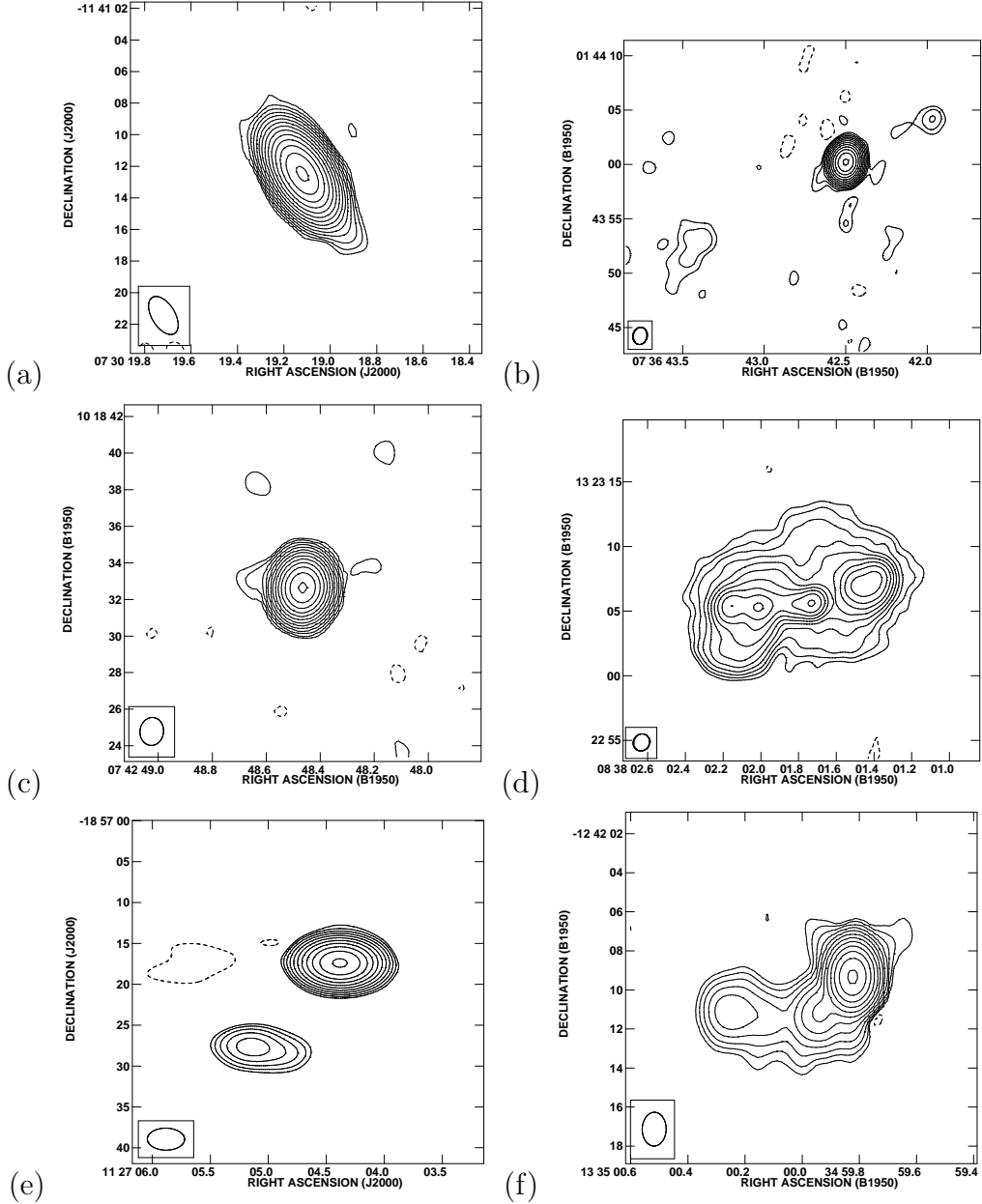


Fig. 13.— New radio images from the VLA archive of (a) 0727–115, (b) 0736+017, (c) 0742+103, (d) 0838+133, (e) 1124–186, and (f) 1334–127. The contours are in percentage of the peak surface brightness and increase in steps of 2. The lowest contour levels and peak surface brightness are, (a) ± 0.01 , $3.15 \text{ Jy beam}^{-1}$; (b) ± 0.042 , $2.33 \text{ Jy beam}^{-1}$; (c) ± 0.021 , $3.61 \text{ Jy beam}^{-1}$; (d) ± 0.17 , $289.3 \text{ mJy beam}^{-1}$; (e) ± 0.085 , $651.2 \text{ mJy beam}^{-1}$; (f) ± 0.042 , $1.94 \text{ Jy beam}^{-1}$.

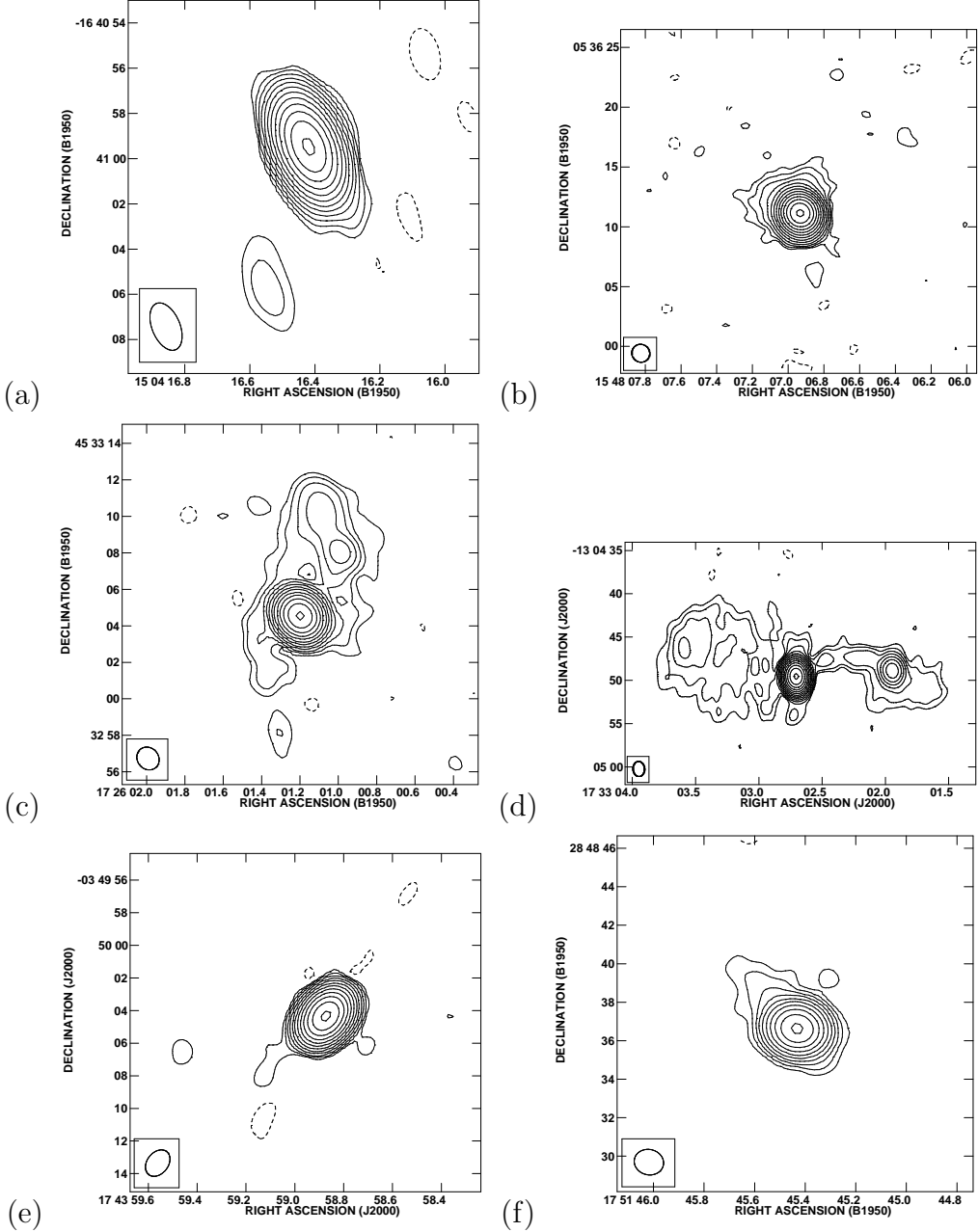


Fig. 14.— New radio images from the VLA archive of (a) 1504–166, (b) 1548+056, (c) 1726+455, (d) 1733–130, (e) 1741–038, and (f) 1751+288. The contours are in percentage of the peak surface brightness and increase in steps of 2. The lowest contour levels and peak surface brightness are, (a) ± 0.042 , $2.36 \text{ Jy beam}^{-1}$; (b) ± 0.021 , $2.09 \text{ Jy beam}^{-1}$; (c) ± 0.042 , $998.9 \text{ mJy beam}^{-1}$; (d) ± 0.021 , $6.11 \text{ Jy beam}^{-1}$; (e) ± 0.042 , $1.68 \text{ Jy beam}^{-1}$; (f) ± 0.17 , $263.5 \text{ mJy beam}^{-1}$.

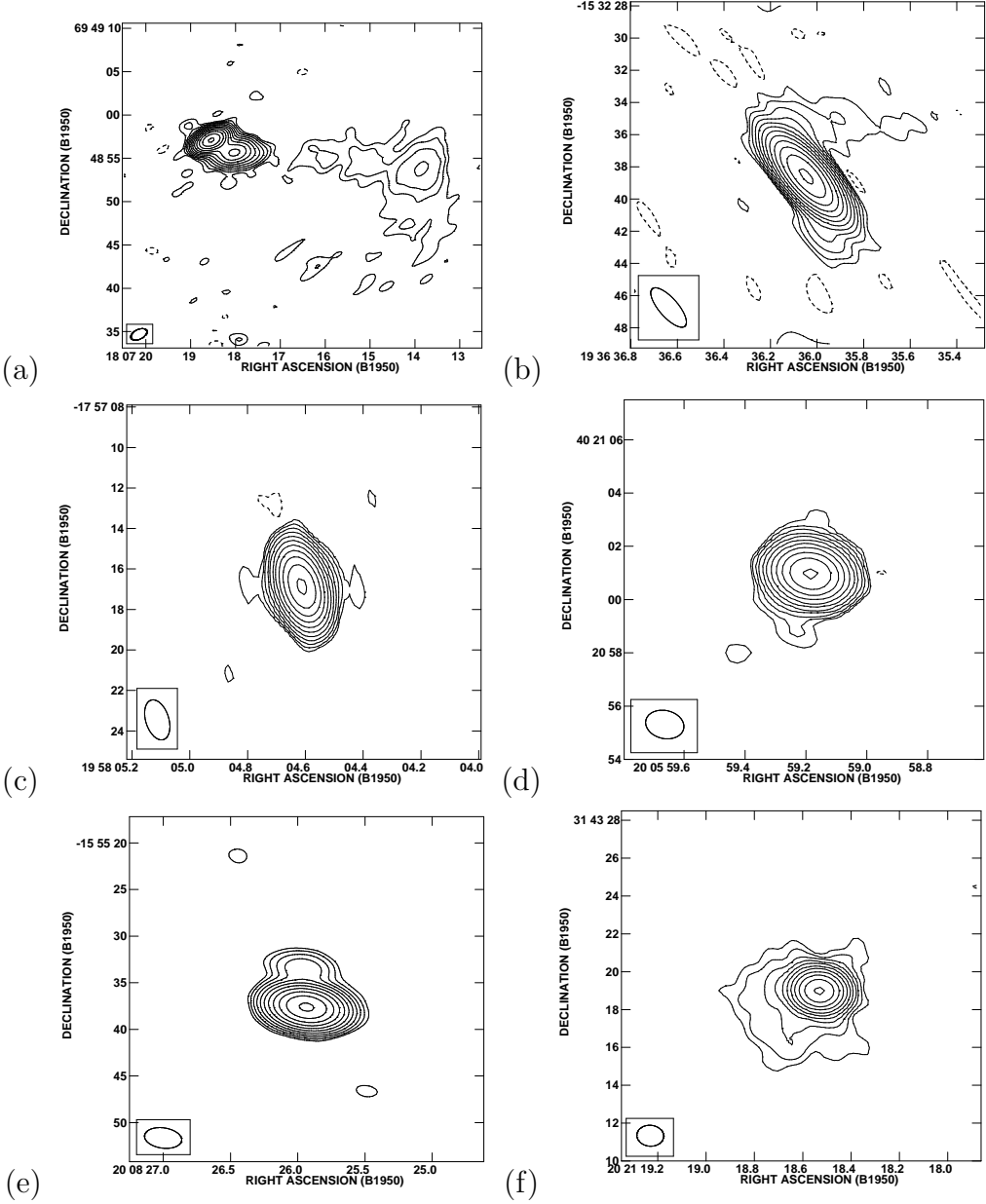


Fig. 15.— New radio images from the VLA archive of (a) 1807+698, (b) 1936-155, (c) 1958-179, (d) 2005+403, (e) 2008-159, and (f) 2021+317. The contours are in percentage of the peak surface brightness and increase in steps of 2. The lowest contour levels and peak surface brightness are, (a) ± 0.042 , $1.14 \text{ Jy beam}^{-1}$; (b) ± 0.085 , $1.05 \text{ Jy beam}^{-1}$; (c) ± 0.085 , $1.77 \text{ Jy beam}^{-1}$; (d) ± 0.085 , $2.43 \text{ Jy beam}^{-1}$; (e) ± 0.085 , $544.5 \text{ mJy beam}^{-1}$; (f) ± 0.085 , $2.97 \text{ Jy beam}^{-1}$.

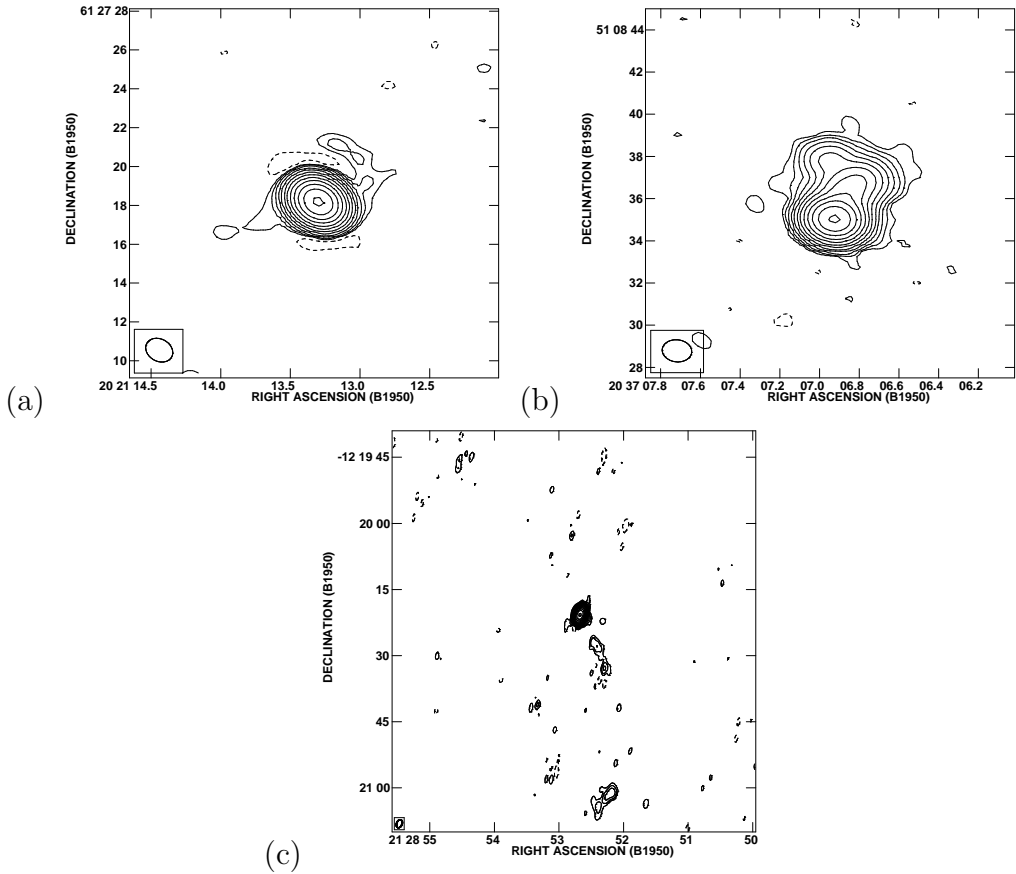


Fig. 16.— New radio images from the VLA archive of (a) 2021+614, (b) 2037+511, and (c) 2128-123. The contours are in percentage of the peak surface brightness and increase in steps of 2. The lowest contour levels and peak surface brightness are, (a) ± 0.042 , $2.64 \text{ Jy beam}^{-1}$; (b) ± 0.042 , $4.61 \text{ Jy beam}^{-1}$; (c) ± 0.042 , $1.37 \text{ Jy beam}^{-1}$.